

AD-A154 043

ACOUSTIC IMAGING SYSTEMS (FOR ROBOTIC OBJECT
ACQUISITION) (U) ROCKWELL INTERNATIONAL THOUSAND OAKS CA
SCIENCE CENTER J M RICHARDSON ET AL. MAR 85 SC5391 5FR

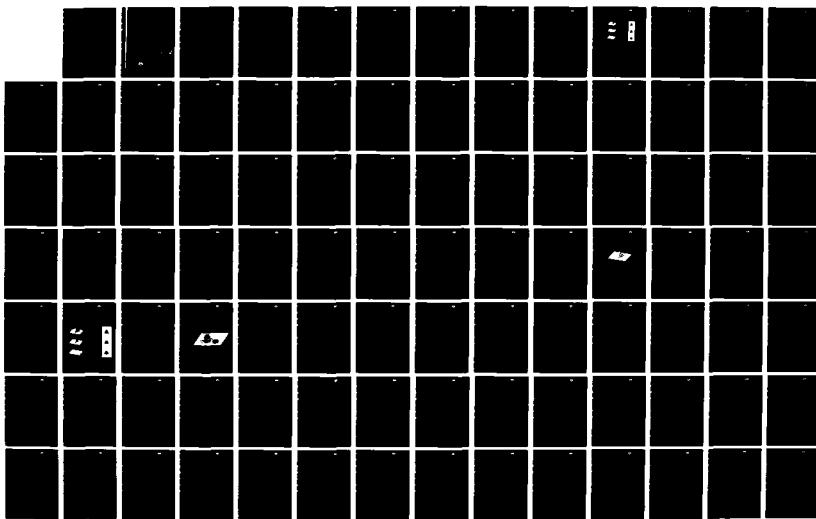
1/2

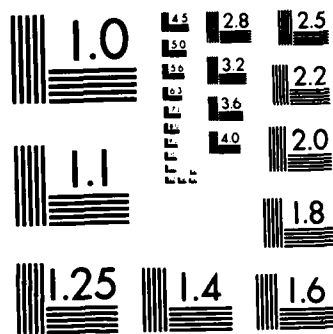
UNCLASSIFIED

N00014-84-C-0085

F/G 17/1

NL





MICROCOPY RESOLUTION TEST CHART
NATIONAL BUREAU OF STANDARDS-1963-A

SC5391.5FR

Copy No. 1

SC5391.5FR

AD-A 154 043

ACOUSTIC IMAGING SYSTEMS (FOR ROBOTIC OBJECT ACQUISITION)

FINAL TECHNICAL REPORT FOR THE PERIOD
December 1, 1983 through November 30, 1984

CONTRACT NO. N00014-84-C-0085
DARPA ORDER NO. 4917

Prepared for

Defense Advanced Research Projects Agency
1400 Wilson Blvd.
Arlington, Virginia 22209

J.M. Richardson, J.F. Martin
K.A. Marsh, J.S. Schoenwald

MARCH 1985

DTIC
ELE 1.2
MAY 22 1985
S A D
A

Approved for public release; distribution unlimited

DTIC FILE COPY



Rockwell International
Science Center

85 04 24 084

UNCLASSIFIED
SECURITY CLASSIFICATION OF THIS PAGE

AD-A154043

REPORT DOCUMENTATION PAGE															
1a. REPORT SECURITY CLASSIFICATION Unclassified	1d. RESTRICTIVE MARKINGS														
2a. SECURITY CLASSIFICATION AUTHORITY	3. DISTRIBUTION/AVAILABILITY OF REPORT Approved for public release; distribution unlimited														
2b. DECLASSIFICATION/DOWNGRADING SCHEDULE															
4. PERFORMING ORGANIZATION REPORT NUMBER(S) SC5391.5FR	5. MONITORING ORGANIZATION REPORT NUMBER(S)														
6a. NAME OF PERFORMING ORGANIZATION Rockwell International Science Center	6b. OFFICE SYMBOL (If applicable)	7a. NAME OF MONITORING ORGANIZATION													
6c. ADDRESS (City, State and ZIP Code) 1049 Camino Dos Rios Thousand Oaks, CA 91360	7b. ADDRESS (City, State and ZIP Code)														
8a. NAME OF FUNDING/SPONSORING ORGANIZATION Defense Advanced Research Projects Agency	8b. OFFICE SYMBOL (If applicable)	9. PROCUREMENT INSTRUMENT IDENTIFICATION NUMBER Contract No. N00014-84-C-0085													
8c. ADDRESS (City, State and ZIP Code) 1400 Wilson Boulevard Arlington, Virginia 22209	10. SOURCE OF FUNDING NOS <table border="1"><tr><th>PROGRAM ELEMENT NO.</th><th>PROJECT NO.</th><th>TASK NO.</th><th>WORK UNIT NO.</th></tr><tr><td>DARPA ORDER NO. 4917</td><td>049-584-(433)</td><td></td><td></td></tr></table>			PROGRAM ELEMENT NO.	PROJECT NO.	TASK NO.	WORK UNIT NO.	DARPA ORDER NO. 4917	049-584-(433)						
PROGRAM ELEMENT NO.	PROJECT NO.	TASK NO.	WORK UNIT NO.												
DARPA ORDER NO. 4917	049-584-(433)														
11. TITLE (Include Security Classification) ACOUSTIC IMAGING SYSTEMS (FOR ROBOTIC OBJECT ACQUISITION) (U)															
12. PERSONAL AUTHOR(S) Richardson, J.M., Martin, J.F., Marsh, K.A., Schwoenwald, J.S.															
13a. TYPE OF REPORT Final Technical Report	13b. TIME COVERED FROM 12/01/83 TO 11/30/84	14. DATE OF REPORT (Yr., Mo., Day) MARCH 1985	15. PAGE COUNT 103												
16. SUPPLEMENTARY NOTATION															
17. COSATI CODES <table border="1"><tr><th>FIELD</th><th>GROUP</th><th>SUB GR.</th></tr><tr><td></td><td></td><td></td></tr><tr><td></td><td></td><td></td></tr><tr><td></td><td></td><td></td></tr></table>	FIELD	GROUP	SUB GR.										18. SUBJECT TERMS (Continue on reverse if necessary and identify by block number)		
FIELD	GROUP	SUB GR.													
19. ABSTRACT (Continue on reverse if necessary and identify by block number) <p>This is a summary of the final report for the first year of effort in DARPA Order No. 4917, entitled "Acoustic Imaging for Robotic Object Acquisition." The long-term objective of the effort is to establish successful approaches for 3D acoustic imaging of dense objects in air to provide the information required for acquisition and manipulation of these objects by a robotic system. The objective was to achieve and demonstrate determination of the external geometry (shape) of such objects with a fixed sparse array of sensors, without the aid of geometrical models or extensive training procedures. Conventional approaches for acoustic imaging fall into two basic categories. The first category is used exclusively for dense solid objects. It involves echo-ranging from a large number of sensor positions, achieved either through the use of a larger array of transducers or through extensive physical scanning of a small array. This approach determines the distance to specular reflection points from each sensor position; with suitable processing an image can be inferred. The second category uses the full acoustic waveform to provide an image, but is strictly applicable only to weak inhomogeneities. The most familiar example is medical imaging of the soft tissue portions of the body where the range of acoustic impedance is relatively small. For dense solid objects in air, both approaches require several hundred transducer positions to obtain a usable image: in the first approach, only a small bandwidth is used effectively; the second approach, significant</p>															
20. DISTRIBUTION/AVAILABILITY OF ABSTRACT UNCLASSIFIED/UNLIMITED <input type="checkbox"/> SAME AS RPT. <input checked="" type="checkbox"/> DTIC USERS <input type="checkbox"/>	21. ABSTRACT SECURITY CLASSIFICATION														
22a. NAME OF RESPONSIBLE INDIVIDUAL	22b. TELEPHONE NUMBER (Include Area Code)	22c. OFFICE SYMBOL													

UNCLASSIFIED

SECURITY CLASSIFICATION OF THIS PAGE

prior information concerning the nature of the object is utilized only partially at best. Therefore, program emphasis was to establish an approach that avoids these deficiencies and obtains useful images with a far smaller set of sensor positions. Four imaging algorithms were developed, implemented and tested; one of the four was conceived during the program and proved to be a significant advance in the state-of-the-art of acoustic imaging. The algorithm, referred to as the "successive unsmoothing" approach, made possible a satisfactory 3D image of a randomly shaped object using a fixed, sparse array of five transducers.

Accession Form		
WTB	R&I	7
DTB	940	
U.S. GOVERNMENT		
JULY 1994		
BY		
Print Name		
AVAILABILITY CODES		
DIST	1	2
A	1	1



UNCLASSIFIED

SECURITY CLASSIFICATION OF THIS PAGE



SC5391.5FR

TABLE OF CONTENTS

	<u>Page</u>
EXECUTIVE SUMMARY.....	1
1.0 INTRODUCTION.....	5
1.1 Nature of This Program.....	5
1.2 Comparison With Other Imaging Techniques.....	6
1.3 Summary of Related Results in IR&D Program.....	7
2.0 OBJECTIVES AND SCOPE.....	9
2.1 Objectives.....	9
2.2 Technical Scope.....	10
3.0 DESCRIPTION OF APPROACH.....	12
4.0 DESCRIPTION OF PROGRESS.....	15
4.1 Comments.....	15
4.2 General Measurement Model.....	16
4.3 Description of First Three Imaging Algorithms.....	21
4.3.1 Comments.....	21
4.3.2 Inclusion Algorithm.....	22
4.3.3 "CLEAN + Thresholding" Algorithm.....	25
4.3.4 Elevation Function Algorithm Using the Conjugate Vector Method.....	28
4.3.5 Results Based Upon Synthetic and Experimental Test Waveforms.....	30
4.4 Discussion of the Fourth Imaging Algorithm.....	38
4.4.1 Comments.....	38
4.4.2 Formulation of the Measurement Model.....	38
4.4.3 Application of Iterative Method.....	39
4.4.4 A Computational Example With a Symmetrical Transducer Configuration.....	44
4.4.5 Two Computational Examples With an Unsymmetrical Transducer Configuration.....	48
4.5 Ambiguity Theorems and Selection of Transducer Configurations.....	53
4.6 Calibration Procedure.....	58
4.6.1 Theoretical Considerations.....	58
4.6.2 Implementation.....	63
4.7 Progress in the Production of Experimental Waveforms.....	64
4.7.1 Suppression of Random Noise.....	64
4.7.2 Suppression of Systematic Noise.....	65



TABLE OF CONTENTS

	<u>Page</u>
4.7.3 Additional Transducer Technology.....	66
4.7.4 Unipolar Transducer Excitation.....	68
5.0 DISCUSSION AND TECHNICAL SUMMARY.....	70
5.1 Nature of the Breakthrough.....	70
5.2 Discussion of the Four Imaging Algorithms.....	72
5.3 Experimental Techniques and Calibration.....	74
5.4 Problems to be Addressed.....	75
6.0 APPENDICES.....	79
7.0 REFERENCES.....	99

LIST OF ILLUSTRATIONS

<u>Figure</u>	<u>Page</u>
1 Unsymmetrical transducer configuration.....	2
2 Application of the iterative algorithm to tetrahedrons of three different assumed heights.....	3
3 Probabilistic imaging methodology.....	13
4 Geometry of experimental setup.....	17
5 Nature of the Kirchhoff approximation.....	20
6 Geometry for scattering.....	24
7 Elevation profile reconstructed from three incident directions using the inclusion algorithm.....	31
8 Reconstruction of the surface of a sphere from synthetic data, using (a) the "CLEAN + thresholding" algorithm, and (b) the elevation function algorithm.....	32
9 Experimental waveforms.....	34
10 Reconstruction from experimental data.....	34



LIST OF ILLUSTRATIONS

<u>Figure</u>		<u>Page</u>
11	Inversion results for (a) hemisphere, (b) tetrahedron, and (c) cube using the "CLEAN + thresholding" algorithm.....	37
12	Assumed squashed tetrahedron.....	45
13	Estimated elevation function for iteration #1.....	47
14	Estimated elevation function for iteration #5.....	47
15	Estimated elevation function for iteration #8.....	47
16	Unsymmetrical transducer configuration.....	49
17	Application of the iterative algorithm to squashed tetrahedrons of three different assumed heights.....	50
18	Imaging with linearized measurement model.....	51
19	Assumed hemispheres.....	52
20	Imaged hemispheres.....	52
21	Stacked plate ambiguity.....	54
22	Ambiguity associated with 3-fold rotation invariance.....	55
23	Geometry of experimental setup.....	58
24	Transducer module with acoustic baffle.....	64
25	Excitation of compressional waves using d13 mode in polymer film transducers.....	67
26	Typical echo waveform obtained with transducer pair.....	67
27	Response of tweeter to square pulse.....	69
28	Response of tweeter to step function.....	69
29	Continuation of the surface integration.....	84



SC5391.5FR

EXECUTIVE SUMMARY

Acoustic Imaging for Robotic Object Acquisition Phase I - Shape Determination with a Sparse Array

This is a summary of the final report for the first year of effort in DARPA Order No. 4917, entitled "Acoustic Imaging for Robotic Object Acquisition." The long-term objective of the effort is to establish successful approaches for 3D acoustic imaging of dense solid objects in air to provide the information required for acquisition and manipulation of these objects by a robotic system. The objective of this first year's work was to achieve and demonstrate the determination of the external geometry (shape) of such objects with a fixed sparse array of sensors, without the aid of geometrical models or extensive training procedures.

Conventional approaches for acoustic imaging fall into two basic categories. The first category is used exclusively for dense solid objects. It involves echo-ranging from a large number of sensor positions, achieved either through the use of a larger array of transducers or through extensive physical scanning of a small array. This approach determines the distance to specular reflection points from each sensor position; with suitable processing an image can be inferred. The second category uses the full acoustic waveforms to provide an image, but is strictly applicable only to weak inhomogeneities. The most familiar example is medical imaging of the soft tissue portions of the body where the range of acoustic impedance is relatively small. For dense solid objects in air, both approaches require several hundred transducer positions to obtain a usable image. In the first approach, only a small bandwidth is used effectively. In the second approach, valuable prior information concerning the nature of the object is utilized only partially at best. Therefore, the program emphasis was to establish an approach that avoids these deficiencies and obtains useful images with a far smaller set of sensor positions.

Four imaging algorithms were developed, implemented and tested; one of the four was conceived during the program and proved to be a significant advance



SC5391.5FR

in the state-of-the-art of acoustic imaging. The algorithm, referred to below as the "successive unsmoothing" approach, made possible a satisfactory 3D image of a randomly shaped object using a fixed, sparse array of five transducers. Figure 1 shows a diagram of the configuration of the measurement system. Figure 2 shows one set of results obtained with the successive unsmoothing imaging algorithm on simulated data. Tetrahedra of three different heights were imaged; the left-hand column shows the original objects. The middle column is a 3D perspective of their images, while the right-hand column is a cross-section of their images taken at a height of 30% of the maximum for each. The tetrahedral shape is quite evident in all three, and the absolute scale is correct. Additional results for other geometries with this algorithm, with the other algorithms, and in one case for actual experimental data are described in the body of the final report.

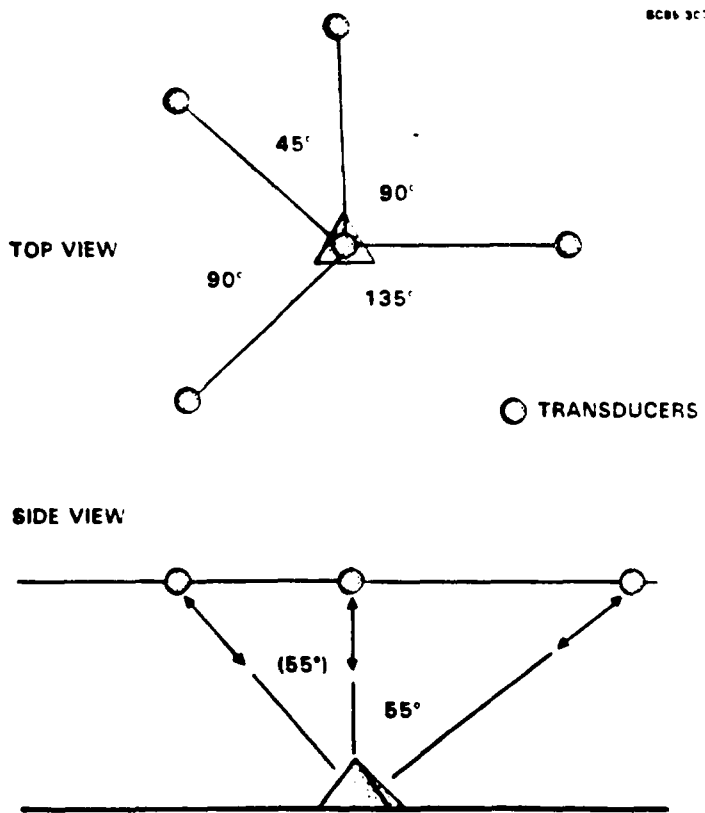


Fig. 1 Unsymmetrical transducer configuration.

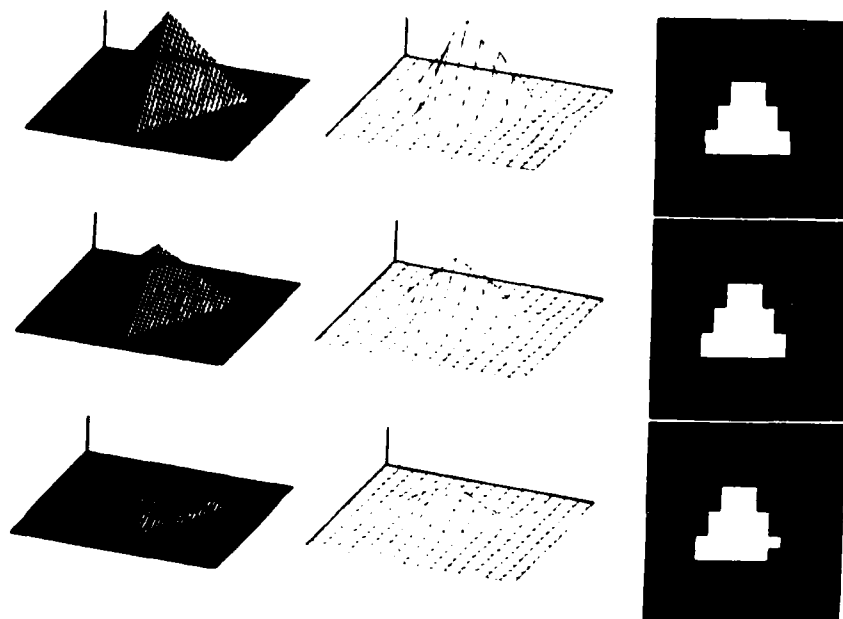


Fig. 2 Application of the iterative algorithm to tetrahedrons of three different assumed heights.

Although the results were obtained under somewhat idealized conditions with respect to noise and bandwidth, they are significant in two ways. First, for a conventional acoustic imaging approach to attain the same performance, either a large-angle array involving several hundred transducers would be required; or a smaller array would have to be physically scanned (moved around) in space. Second, the images in Fig. 2 exhibit a substantial degree of super-resolution, that is, a resolution approximately a factor of two beyond the diffraction limit for the frequency range used.

This level of performance is made possible by three basic ingredients. The first is that the imaging algorithm is coherent: it uses the entire waveform instead of just one or two extracted features. Second, the bandwidth of the acoustic waves is very large: for Fig. 2, the frequency range was 1 to 40 kHz. The advantage of the large bandwidth is that the longer wavelengths define



Rockwell International
Science Center

SC5391.5FR

global features, while the shorter wavelengths obtain a high level of resolution. Third, a probabilistic technique was used to perform the inversion of the acoustic data to get the image. This allows straightforward incorporation of a physical model of the scattering process, a statistical model of the measurement error, and a simple statistical model of the possible objects. These models, sometimes referred to as "a priori" information, made no assumptions about the object's specific geometry, except that it was to have no undercut surfaces.

The significance of this work is that it makes possible, for highly reflective objects, the formation of adequate images with arrays that heretofore were considered too sparse for imaging. In addition, the quality of images obtained with larger arrays should be improved substantially by using some of these techniques. Finally, because the results apply to coherent imaging in general, systems that image with other forms of energy such as radar can also benefit.



SC5391.5FR

1.0 INTRODUCTION

1.1 Nature of This Program

This program represents a critical step in an effort to develop advanced acoustic 3-dimensional imaging concepts optimized for applications in manufacturing systems involving robots in particular and intelligent machines in general. A theme characteristic of this work is the role of a priori information in the improvement of imaging algorithms. The improvement could be imaging performance for a given measurement system or a simpler measurement system (i.e., a system involving a sparser set of measurements) for a given level of performance. Clearly many possibilities exist between these extremes. In the imaging of solid objects in air, we use the obvious, but important, a priori information that every volume element in space is occupied either by air or a part of the solid object; and, that the solid object has an enormous acoustical impedance compared with that of air. This kind of a priori information enables us to use a relatively small number of fixed transducers, at least in high signal-to-noise-ratio situations. Furthermore, one can hope to attain a significant amount of k-space interpolation and a certain degree of super-resolution; i.e., attaining a fidelity of estimated geometry beyond that given by conventional imaging procedures.

One approach to acoustic imaging is to scan the object of interest by mechanically moving a single transducer, as in the work of Jarvis (1982) and Schoenwald and Martin (1982). This technique is rather slow and results in poor lateral resolution if the scan pattern is planar. Although in principle the mechanical scanning system could be replaced with a phased array, such an array would require a large number of transducers to achieve a sufficiently large aperture to overcome diffraction limitations, and to provide a sufficient diversity of viewing directions. However, successful 3-dimensional acoustic imaging can use relatively modest arrays provided efficient use of a priori information of the complete waveforms is made.



1.2 Comparison With Other Imaging Techniques

In this section we present some observations that compare our acoustic imaging techniques with other non-acoustic imaging techniques, in particular optical imaging. In the last section, we alluded briefly to a comparison of our acoustic imaging technique with other, older approaches to acoustic imaging.

Although considerable success has been obtained with optical techniques for 3-dimensional imaging in robotics, in some situations, acoustic techniques might be more appropriate. Examples include smoky atmospheres, undersea environments, highly polished or transparent objects or surface objects with irregular coloring. We are not attempting a broad survey of the various optical imaging techniques currently used in robotics. However, defining the word optical to imply the use of electromagnetic waves in the visible, we can state that many optical imaging systems used in robotics depend upon a certain amount of diffuse scattering from the surface of the object. Thus, nontransparent objects with optically smooth surfaces would present substantial difficulties to optical imaging systems dependent on a certain degree of diffuse scattering. Transparent objects (whose surfaces must be smooth in order to be transparent) present even greater difficulties.

One can imagine optical vision systems specially designed to deal with optically smooth surfaces of nontransparent objects. However, with a dense array of illumination sources operating simultaneously or in some sequential mode, the signal processing problems associated with most conceivable sensor systems appear to be quite cumbersome for estimating the full external geometry. Even with the more modest objective of determining some kind of silhouette, many sources of confusion must be resolved. An optical vision system designed to deal with transparent objects appears to be a challenge of even greater magnitude.

Although the state-of-the-art of acoustic 3-dimensional imaging of hard objects in air is in a comparatively embryonic state, certain characteristics of this approach suggest that it may find a viable niche either as a stand-alone system or in combination with an existing optical vision system. At least two



Rockwell International
Science Center

SC5391.5FR

case of scattering of elastic waves from a spherical void in a solid is very similar for longitudinal waves as far as the impulse response function (IRF) is concerned, except for a change in sign of the amplitude. In Fig. 5 we show the IRFs of a spherical void in an elastic solid for both exact theory and the approximate Kirchhoff theory. The results are plotted with an arbitrary scale of amplitude versus the dimensionless time variable ct/a , where a is the sphere radius. The clearly indicated Kirchhoff IRF is composed of horizontal and vertical line segments. The exact IRF for $ct/a > -2$ is a continuous curve. Note that the Kirchhoff and exact IRFs start with identical δ -functions with negative polarity at $ct/a = -2$ followed immediately by identical step functions. At later times the two IRFs diverge from each other significantly. The first severe divergence is the downward discontinuity in the Kirchhoff IRF at $ct/a = 0$. This is associated with the beginning of the acoustical shadow zone. At still later times the Kirchhoff IRF has a zero amplitude while the exact IRF undergoes several undulations associated with the propagation of surface-skimming bulk waves around the backside of the sphere.

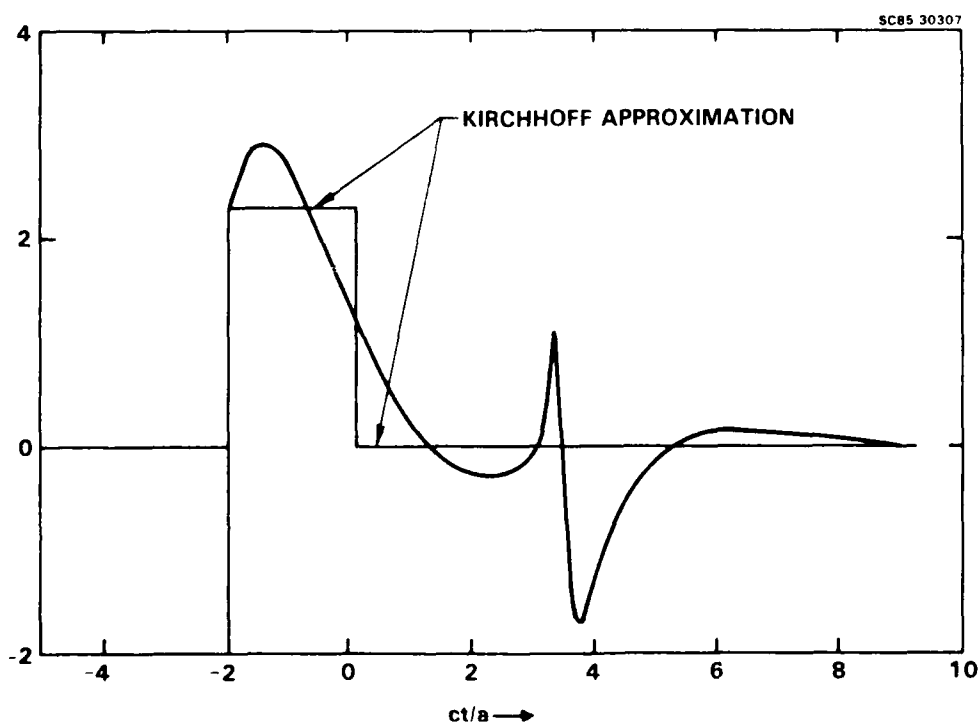


Fig. 5 Nature of the Kirchhoff approximation.



SC5391.5FR

$$f(\omega, \vec{e}) = -\alpha\omega^2 p(\omega) \int d\vec{r} \exp(2i\omega c^{-1} \vec{e} \cdot \vec{r}) \\ \times [\Gamma(\vec{r}) + \Gamma_{sh}(\vec{r}, \vec{e})] + v(\omega, \vec{e}) \quad (3)$$

in which the frequency ω takes a discrete set of values that are multiples of $2\pi/T$ where T is the observation time. The function $f(\omega, \vec{e})$, $v(\omega, \vec{e})$, and $p(\omega)$ are simply the Fourier transforms of $f(t, \vec{e})$, $v(t, \vec{e})$ and $p(t)$.

When the object is resting on a table, the characteristic function $\Gamma(\vec{r})$ in (1) is replaced by $\Gamma(\vec{r}) + \Gamma_{tab}(\vec{r})$ where $\Gamma_{tab}(\vec{r})$ is the characteristic function of the table. Suppose simply that the object does not have an acoustical shadow and thus $\Gamma_{sh}(\vec{r})$, carried over from (1) to (2), now represents solely the acoustical shadow of the table. Furthermore, if the incident wave form f^i is defined as the measured scattered wave from the table without the object present, and the scattered waveform f^s is defined as the correction due to the presence of the object, we can then write the correspondences

$$f^i + f^s \Leftrightarrow \Gamma + \Gamma_{tab} + \Gamma_{sh}$$

$$f^i \Leftrightarrow \Gamma_{tab} + \Gamma_{sh}$$

and because of the general linear dependence of the waveforms on the characteristic functions, it follows that

$$f^s \Leftrightarrow \Gamma .$$

In other words, with the present situation the scattered waveform is given by (1) or (2), with only the object characteristic function present under the integrals. This result is mathematically equivalent to the Born approximation.

At this point we turn to the important question of the validity of the Kirchhoff approximation for the scattering process. We compared the exact theory and the Kirchhoff approximation in the case of pulse-echo scattering of acoustical waves from a rigid sphere. Unfortunately, we do not have the results of the exact theory easily available for this case. However, the "opposite"



SC5391.5FR

$\Gamma(\vec{r})$ = characteristic function* of the body,

$\Gamma_{sh}(\vec{r}, \vec{e}^+)$ = characteristic function* of the acoustical shadow domain
(determined in the geometrical optics limit),

$\vec{r}, d\vec{r}$ = 3D position vector and differential volume element,
respectively,

c = velocity of sound in the host medium,

α = constant depending on the properties of the host medium.

A more basic analysis of the scattering process (see Appendix A) yields the result

$$\alpha = \frac{1}{\pi c^2} . \quad (2)$$

The complete specification of the measurement model requires the specification of the a priori statistical properties of the scatterer (as represented by $\Gamma(\vec{r})$) as well as the additive noise $v(t, \vec{e})$. We address this question later in connection with specific applications.

In a realistic algorithm the continuous integration on \vec{r} would be replaced by a sum on a discrete lattice extending over the localization domain. Furthermore, the limit would be discretely sampled. We have not introduced these modifications into the general model at this stage in order to provide a convenient point of departure for the derivation of other representations of the general model.

The importance of these modifications is the transformation from the time domain to the frequency (temporal) domain. Equation (1) is thus replaced by (see Appendix A)

*We have changed the notation here relative to that used in Appendix A.



Rockwell International
Science Center

SC5391.5FR

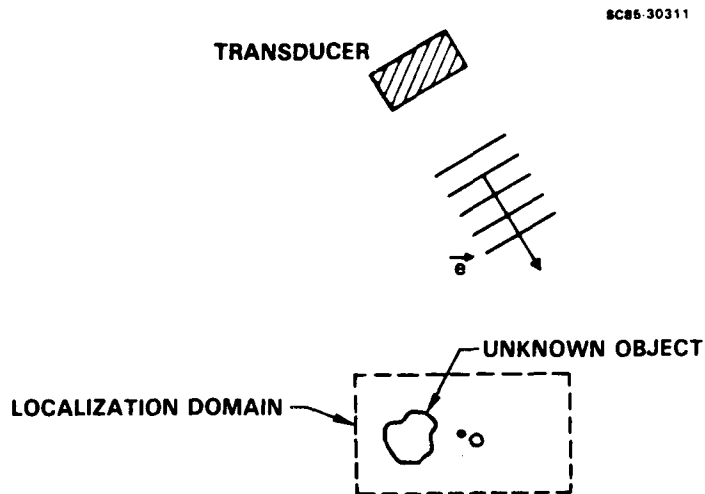


Fig. 4 Geometry of experimental setup.

$$f(t, \vec{e}) = \alpha \int d\vec{r} p''(t - 2c^{-1} \vec{e} \cdot \vec{r})(R(\vec{r}) + r_{sh}(\vec{r}, \vec{e})) + v(t, \vec{e}) \quad (1)$$

using the Kirchhoff approximation for the scattering process. The integration on \vec{r} spans the localization domain. In this model we have assumed that the localization domain and the transducer are in the far-field of each other. The symbols in the above expression are defined by

$f(t, \vec{e})$ = possible measured scattered waveform at time t and incident direction \vec{e} ,

$v(t, \vec{e})$ = stationary Gaussian random process representing measurement error, contributions of external noise sources, etc.,

$p(t)$ = measurement system response function, i.e., the waveform obtained when a fictitious point scatterer with a δ -function impulse response function (i.e., the impulse response function is given by $R(t) = \delta(t)$) is placed at the origin of the laboratory coordinate system. The function $p''(t)$ is the second time derivative of $p(t)$,



SC5391.5FR

From the standpoint of imaging performance, the most satisfactory imaging algorithm was the fourth. This algorithm is based on an iterative method that involves an initial smoothing of both the waveform and the measurement system response function, followed by successive unsmoothings and linearizations with respect to corrections in the estimated elevation function. Other parameters in the measurement model may be allowed to vary in the iteration process.

Most of the test data used to evaluate these algorithms were generated theoretically. The second algorithm was also tested with actual experimental data; results are discussed later.

Clearly, the development of an actual imaging system requires advances in the techniques of making accurate acoustical scattering measurements. Our efforts to improve both the experimental hardware and the associated signal conditioning (including calibration techniques) are fully described.

Later in the program, we discovered some important ambiguity theorems that have a direct bearing on the selection of incident directions. A more thorough discussion is given in the latter part of this section. Many important ambiguities are associated with certain kinds of symmetry; thus in the choice of an experimental set-up, these symmetries are to be avoided as much as possible.

4.2 General Measurement Model

The ensuing discussion of imaging algorithms should be simplified by the presentation of a general measurement model; all the special models in later sections are special cases.

A schematic version of an experimental set-up is presented in Fig. 4. Here, the geometrical description of a single pulse-echo measurement of a general object is illustrated. In Appendix A we have shown that the general measurement model for the pulse-echo scattering of acoustical waves from a perfectly rigid object can be expressed in the form



SC5391.5FR

4.0 DESCRIPTION OF PROGRESS

4.1 Comments

In this section we describe progress made during the first year of the DARPA supported program on acoustic imaging of solid objects in air in the context of robotic acquisition. As stated before, imaging here means the determination of the external geometry of the object. In this program considerable (but not exclusive) emphasis was put on flat-bottomed objects on a highly reflective table where the upper surface of the object is represented by a single-valued elevation function.

Here, we describe four distinct imaging algorithms. The first two (i.e., the inclusion algorithm and the "CLEAN + thresholding" algorithm) are based on the representation of the object by a characteristic function. Thus, any conceivable object geometry can be represented (within the limitations imposed by the voxel size). The third and fourth algorithms (i.e., the elevation function algorithm using the conjugate vector method and the elevation function algorithm using an iterative method) are based on the representation of the object by an elevation function (as we have already implied). Because of the difficulty of dealing with multiple-valued elevation functions we have temporarily limited our scope to cases involving flat-bottom objects whose upper surfaces are represented by single-valued elevation functions. We have also limited our scope to cases in which acoustic shadowing is either absent or inconsequential.

Tentative findings are that the first three algorithms were deficient in various ways. Nevertheless, we present a full discussion, since each has certain positive features that relate to at least two kinds of uses: (a) some of them were improved in one way or another to yield a satisfactory algorithm (e.g., conceivably the first or third can be so improved), and (b) some of them can be used in conjunction with the fourth algorithm with a net benefit (e.g., the second algorithm can be used to provide a good initial guess for the iteration procedure in the fourth algorithm).



SC5391.5FR

The input at the top of the central unit (labelled "objective") also has an off-line nature and determines the nature of the final stage of the decision process. If the objective is to achieve the best score (i.e., the greatest fraction of correct images, using a certain tolerant comparison procedure, in an ensemble of tests) then the best image is the most probable one given the results of measurement. This procedure was mentioned at the beginning of this discussion. Although many other possible objectives can be formulated, the above is perhaps the most appropriate and the most convenient.

The remaining input is the set of measured waveforms, and clearly this has an on-line (i.e., approximately real-time) nature. Generally, this input is composed of a suitably digitized version of the transducer outputs with time or frequency discretization accompanied by the appropriate amplitude quantization. The principal output is the estimated image (representing the 3-dimensional external geometry of the object) while usually of an on-line nature. Several ways of representing this output will be described later. This output should be accompanied by an ancillary output (labelled "confidence measure") that gives some indication of estimated image quality, i.e., how the estimated image deviates from the true image. Since we do not know what the true image is, we must rely on some kind of statistical measure, e.g., the a posteriori covariance matrix.

The above discussion of probabilistic imaging methodology provides a clear picture of the conceptual aspects of the problem. However, many problems are entailed in the implementation of an imaging concept; i.e., the realization of the concept in terms of practical software and hardware. The investigation and eventual solution of these problems (although within a limited scope) are the main substance of the first-year effort. Section 4.0 presents a detailed discussion of these matters.

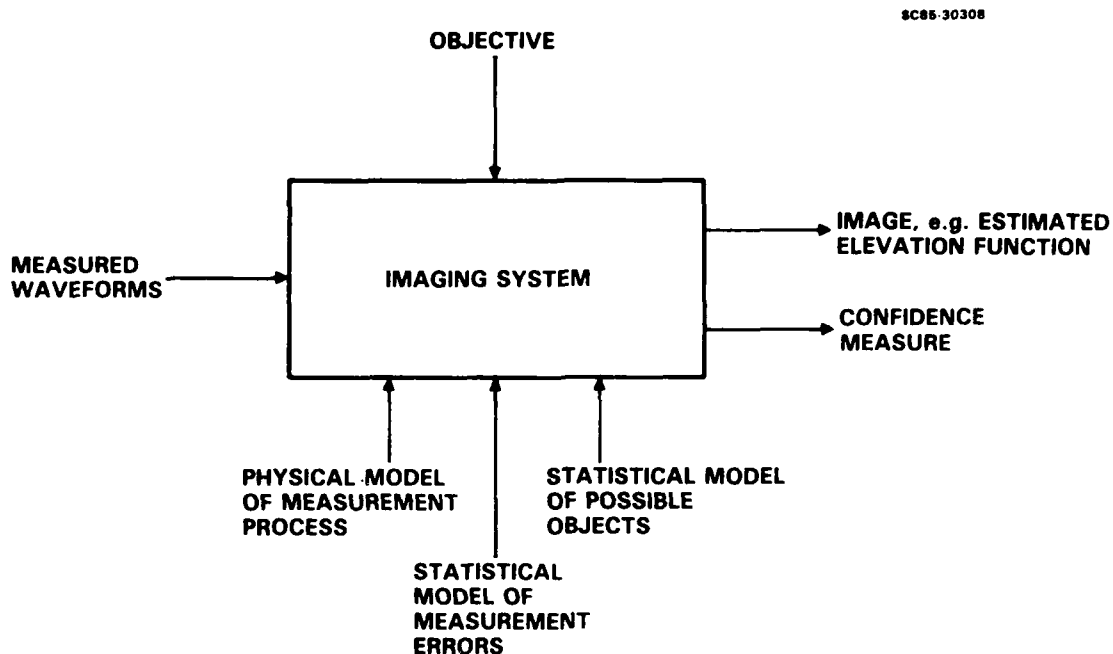


Fig. 3 Probabilistic imaging methodology.

given object in the absence of experimental error. It contains several component parts; i.e., a model of the scattering process (i.e., the Kirchhoff theory of scattering), the input-output characteristics of the transducers operating in both transmit and receive modes, and a representation of the propagation of acoustical waves from the transducer to the scattering object and back. The statistical model of the experimental errors requires no further discussion at this point. The model of possible objects is a crucial part of the measurement model and is responsible for the advancement of our methodology beyond that of conventional imaging. The main point is that this part represents not general inhomogeneities; but very special inhomogeneities in which each cell (or voxel) in space is occupied either by air or object with specific a priori probabilities. The acoustical impedance of the material in the object (or at least on its surface) is assumed to be so large compared with that of air that it can be taken as infinite.



SC5391.5FR

3.0 DESCRIPTION OF APPROACH

Our approach to acoustic imaging is based on two ideas: (1) the use of all available information, both in the measured signal and in the mathematical model representing various kinds of a priori information; and (2) the extension of the range of application of the Kirchhoff approximation to include frequencies where significant contributions are made by diffraction from the global geometry of the illuminated part of the object surface.

All available information is pursued most appropriately within the framework of the optimal probabilistic methodology. In the past the latter has been applied successfully to inverse problems involving various levels of a priori information represented by certain statistical scatterer models; e.g., a Gaussian random process, a Gaussian random process modified by a positivity constraint, and an inclusion with known material but unknown boundary (Richardson and Marsh 1982a).

The extension of the range of the Kirchhoff approximation beyond the specular reflection regime has been carried out by a number of investigators. For example, Quentin and coworkers have used single ultrasonic backscatter measurements of rough surfaces to determine elevation histograms effectively, an "incomplete image" which could be made complete by incorporating sufficient direction diversity (deBilly 1980, Cohen-Tenoudji 1982).

At this point, we describe the probabilistic imaging methodology in more detail. At an abstract level this methodology is based on a complete model of the measurement process (including random aspects) to determine the most probable image given the actual results of measurement. A more detailed representation of this decision procedure is given in Fig. 3. We will first discuss the inputs into the central decision making unit (labeled "imaging system").

Three inputs of an off-line nature enter the bottom of the central unit; namely, a physical model of the measurement process, a statistical model of measurement errors, and a statistical model of possible objects. The first model deals with the physical nature of the total measurement process for a



Rockwell International
Science Center

SC5391.5FR

and two-valuedness). In fact, the nonparametric model does not necessarily correspond to a single object within the localization domain; any number of separate objects may exist. Second, actual emphasis near the end of the first year was limited to flat-bottomed objects resting on a reflective table where the upper surface of the object is represented by a single-valued elevation function without significant acoustical shadowing. This corresponds to a much more restrictive scope than that implied by statements 3 and 4.



SC5391.5FR

2.2 Technical Scope

The scope of this first year of the program is defined by the following statements:

1. Each transducer makes a pulse-echo scattering measurement of the solid object.
2. Each transducer is in the far field of the localization domain and vice versa. The localization domain is a volume outside of which no part of the object is known to exist a priori.
3. The object rests on a reflective table or is supported in mid-air. A strong emphasis was placed on the former situation.
4. The object and its acoustical shadow can be approximately modeled by a single-valued elevation function.
5. Both synthetic and experimental test data will be employed for producing images of the objects.
6. The output of the imaging algorithm will be given in the form of a conventional three-dimensional hidden-line presentation of the top elevation function (i.e., in the case of multiple-valued elevation functions the maximum elevation at each point in the horizontal plane).

A number of clarifying comments should be made relative to the above statements. First, the possible objects are represented by a statistical ensemble of solid models confined within the specified localization domain which may possibly be much larger than the objects. The solid models are nonparametric in nature (i.e., all possible models contained within the localization domain are to be considered, perhaps within certain additional restrictions such as positivity



SC5391.5FR

2.0 OBJECTIVES AND SCOPE

2.1 Objectives

The general objectives of the present program were:

1. To develop an acoustical imaging concept for determining the 3-dimensional geometry of solid objects in air with a measurement system involving a relatively sparse set of transducers. Each object is assumed to rest on a highly reflective table or to be supported in mid-air. A number of alternative realizations in terms of software and hardware are envisioned.
2. To develop ultimately an acoustical system concept for the recognition (i.e., determination of type, orientation and position) of solid objects resting on a table.

The objective for the first year was the same as the first general objective except for a significantly restricted technical scope (see the next section), as follows:

3. Within the technical scope defined in the next section, to develop an acoustical imaging concept for determining the 3-dimensional geometry of solid objects which rest on a reflective table or are supported in mid-air. To achieve a realization of the concept in terms of software and hardware, where the latter will be computer simulated in the early phases of the program. To demonstrate the operation of the concept for simple objects and to compare the results with those obtained by conventional acoustic imaging.

As stated in Section 3.0, this objective can be attained by using both synthetic and experimental test data. Actually, we have put a heavy emphasis on the former.



SC5391.5FR

2. Application of the Pontryagin maximum principle (PMP) to the inverse problem pertaining to the scattering from rigid objects in air, either isolated or resting on a reflective table. This approach appears to have a reasonable chance of yielding an exact solution to the inverse problem in a form that is both analytically and computationally tractable. In particular, we believe that this tractability almost surely could be obtained for the kinds of scatterers (flat-bottom objects on a reflective table) that are appropriately represented by a single-valued elevation function. This methodology has been applied recently to a simple, but unrelated, case of a fluid with uniform density but nonuniform sound velocity. A paper discussing this result has been prepared by Richardson (1985) and has been accepted for publication.
3. Investigations of the conjugate vector method in cases where the operations of maximum and minimum are not obviously interchangeable. In the case of discrete-values state vectors, the method has often been successful, but without rigorous mathematical justification. We have recently established the conditions under which the method is valid. A communication discussing this result will be forthcoming in the near future.



SC5391.5FR

characteristics are worthy of note: (a) the various scattered waves depend only on the gross external geometry of the object (not on its color or fine-grained texture) and (b) the scattered waves associated with the pulse-echo measurement by a given transducer emphasize the extension of the illuminated surface in the range direction.

The above comparison of optical and acoustical vision systems does not compare the uses of electromagnetic and acoustic waves. Rather, it compares the use of certain noncoherent properties of very short wavelength waves with the use of coherent properties of waves whose spectrum of wavelengths is matched in some appropriate way to the spectrum of relevant characteristic lengths of the objects. One could imagine the latter approach being implemented in terms of microwaves and the former in terms of acoustical waves (if attenuation were not too severe).

1.3 Summary of Related Results in IR&D Program

Projects supported by Rockwell International IR&D funds involved investigations that were antecedent to the present DARPA supported program and were ancillary to this program. These IR&D investigations are differentiated from the DARPA effort in that they are concerned with the generic and basic aspects of problems in the general field of imaging and inversion. Although these investigations lie outside of the strictly defined scope of the DARPA contract, a brief discussion of them is not out of place here. Some of these investigations are listed below:

1. Further investigation of the exact boundary integral equation (BIE) describing the scattering of acoustic waves from rigid objects resting on a reflective table. We hope to find an approximation that is analytically and computationally tractable but, at the same time is an improvement on the Kirchhoff approximation. We also hope that this investigation will shed more light on the nature of the Kirchhoff approximation and its limits of validity.



SC5391.5FR

These observations support the contention that the Kirchhoff theory is really valid for short times, not simply at high frequencies. Another interesting property of the comparison is that the divergences are most serious when both theories have relatively low amplitudes. We hasten to emphasize that for objects with more-or-less flat bottoms sitting on a table the actual scattering process should involve relatively little contribution from surface-skimming bulk waves propagating around the backside (i.e., the lower surface). The treatment of acoustical shadow zone is a sort of theoretical makeshift and is not the result of a systematic theoretical development. A more accurate treatment of waves in the shadow zone (defined in the geometrical optics limit) is clearly needed.

One important remaining aspect of the Kirchhoff approximation that does not exist for convex objects is the presence of possible multiple reflections. Such processes could contribute significantly to pulse-echo measurements in the case of concavities, grooves, exterior surfaces meeting at approximately right angles, etc. However, in most cases, the imaging algorithm will interpret such scattering processes to have been caused by spurious scatterers in the interior of the object.

4.3 Description of First Three Imaging Algorithms

4.3.1 Comments

As discussed in Section 3.0, our algorithms for imaging solid objects in air utilize measurements consisting of pulse-echo waveforms taken in a small number of incident directions, together with probabilistic inversion procedures which make use of a priori information about the statistical nature of the scatterer. The most important piece of available prior information in the case of solid objects in air is that the discontinuity in acoustic impedance is so large that the scattering properties of the object are essentially independent of the actual value of acoustic impedance, and depend only on the external geometry of the object. Thus, we can write an acoustic measurement model in which the entire scene is represented by a function that takes only two possible values everywhere in space, which may be defined to be 0 and 1. Such a function



SC5391.5FR

is known as a characteristic function. In many cases, however, knowing this function everywhere may not be necessary; knowing the elevation function of the visible surface as seen from some viewpoint may suffice.

In the case of certain types of objects sitting on a flat surface, the entire geometry of the scattering system can be described in terms of an elevation function which is single-valued at each horizontal location. We refer to such a function as a single-valued elevation function.

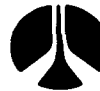
In this section we describe three imaging algorithms. The first two use the characteristic function representation, and the last one uses the single-valued elevation function representation. The first of these algorithms, referred to as the "inclusion algorithm," was developed first for NDE, and applied to the imaging of weakly scattering inclusions in solids, using the Born approximation. As will be explained below, a simple modification of the algorithm enables its application to the imaging of strong scatterers in air, using the Kirchhoff approximation.

4.3.2 Inclusion Algorithm

A probabilistic technique valid for the case of weakly scattering inclusions has been proposed by Richardson and Marsh (1983a). This technique is based on the Born approximation and utilizes pulse-echo measurements. Each voxel of the image is considered an independent random process, with various assumed statistical distributions of possible acoustic impedance values. One such distribution allows each pixel to have only two possible values, namely 0 or 1, and corresponds to the situation whereby an inclusion of known material exists within an unknown boundary. The measurement model is of the form:

$$f(t, \vec{e}) = \alpha \sum_{\vec{r}} p''(t - \frac{2\vec{e} \cdot \vec{r}}{c}) r(\vec{r}) \delta \vec{r} + v(t, \vec{e}) \quad (1)$$

where f represents the measured waveform as a function of time t and incident direction \vec{e} , α is a parameter dependent on the material properties, $\delta \vec{r}$ is a volume increment, $p(t)$ is the reference pulse, c the velocity of sound in the host medium, v represents the noise (assumed to be Gaussian with variance σ_v^2), and



SC5391.5FR

$\Gamma(\vec{r})$ is the characteristic function for the inclusion (equal to 1 inside the inclusion and 0 outside) as a function of the position vector \vec{r} . The inversion technique consists of finding the image Γ which maximizes the conditional probability $P(\Gamma|f)$, and which can be obtained by minimizing a variational function ψ with respect to a conjugate vector w , where:

$$\begin{aligned}\psi = \sum_{t, \vec{e}} & \left[\frac{1}{2} \sigma_v^2 w(t, \vec{e})^2 - w(t, \vec{e}) f(t, \vec{e}) \right] \\ & + \sum_{\vec{r}} (\lambda(\vec{r}) 1(\lambda(\vec{r}) + \ln \frac{P_1}{1 - P_1}))\end{aligned}\quad (2)$$

such that

$$\lambda(\vec{r}) = \alpha \sum_{t, \vec{e}} p''(t - \frac{2\vec{e} \cdot \vec{r}}{c}) w(t, \vec{e}) \delta \vec{r} \quad (3)$$

where P_1 represents the a priori probability of a pixel having the value 1 and $1(\cdot)$ represents the unit step function. The most probable image is then given by

$$\hat{\Gamma}(\vec{r}) = 1(\lambda(\vec{r}) + \ln P_1/(1 - P_1)) \quad (4)$$

The zero-crossings of the offset λ function thus represent the boundary of the inclusion. This algorithm, which we will refer to as the "inclusion algorithm", is not directly applicable to the case of acoustic imaging in air since the acoustic impedance of a solid object is orders of magnitude greater than that of air. Hence, the Born approximation would not be valid. Provided the scatterer behaves as a rigid body, the Kirchhoff approximation would give a reasonable representation of the scattering process. The measurement model would then be of the form:

$$\begin{aligned}f(t, \vec{e}) = \alpha \sum_{\vec{r}} & p''(t - \frac{2\vec{e} \cdot \vec{r}}{c}) [\Gamma(\vec{r}) + r_{sh}(\vec{r}, \vec{e})] \delta \vec{r} \\ & + v(t, \vec{e})\end{aligned}\quad (5)$$



SC5391.5FR

where $\Gamma_{sh}(\vec{r}, \vec{e})$ represents the characteristic function for the shadow zone, determined (in the geometrical optics limit) for the incident wave propagating in the direction \vec{e} . The geometry of the shadow zone is illustrated in Fig. 6. Γ_{sh} also depends upon the geometry of the object. An additional point to note is that whereas the Born approximation is exact in the weak-scattering limit, the Kirchhoff approximation is not exact in any physical limit; thus, the noise term v in Eq. (5) should be interpreted as including the model error in addition to the measurement error.

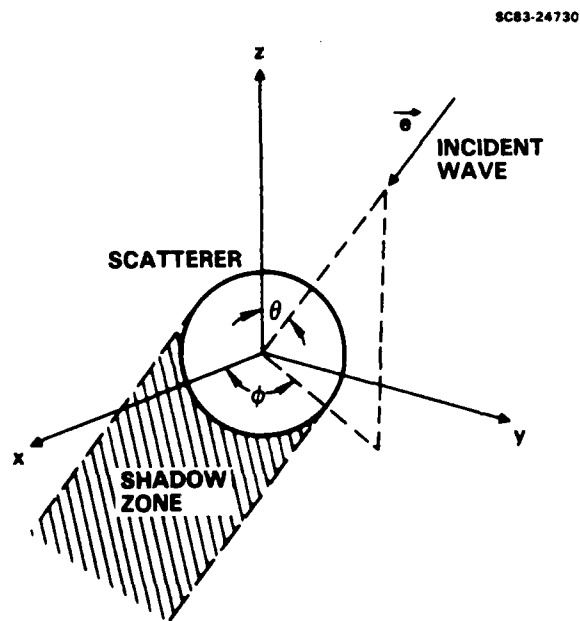


Fig. 6 Geometry for scattering.

The close resemblance of Eq. (5) to Eq. (1) suggests that we could use the same basic inversion technique, i.e. the inclusion algorithm, provided we can deal in a satisfactory manner with the shadow zone. One possible method is to use a measurement configuration such that the effect of the shadow zone cancels out in the measurement model. This corresponds to the case of measurements made with pairs of oppositely-directed transducers. If we define

$$\begin{aligned} f_+(t, \vec{e}) &= f(t, \vec{e}) + f(-t, -\vec{e}) \\ v_+(t, \vec{e}) &= v(t, \vec{e}) + v(-t, -\vec{e}) \end{aligned} \tag{6}$$



SC5391.5FR

then provided $p(t)$ is an even* function, we can re-express Eq. (5) in the form (Richardson and Marsh 1983b):

$$f_+(t, \vec{e}) = \alpha \sum_{\vec{r}} p''(t - \frac{2\vec{e} \cdot \vec{r}}{c}) \Gamma(\vec{r}) \delta \vec{r} + v_+(t, \vec{e}) \quad (7)$$

Since Eq. (7) is identical mathematically to Eq. (1), the inclusion algorithm would be a valid inversion technique. The disadvantage, of course, is that the object to be imaged be surrounded by oppositely-directed pairs of transducers. This is often feasible for NDE but rather unreasonable for robotics. An alternative way of dealing with the shadow zone is to make the artificial assumption that the shadow zone is the same for all measured incident directions. If the measurements are all within a limited angular sector, this may not be too bad an approximation. Some error will exist still, but we would hope that it could be satisfactorily included in $v(t, \vec{e})$.

4.3.3 "CLEAN + Thresholding" Algorithm

An alternative to the inclusion algorithm is the CLEAN algorithm (Hogbom 1974), used extensively in radio astronomy for deconvolving the point spread response from images made by radio interferometers.

For this algorithm, more conveniently we work in the frequency domain, and we rewrite the measurement model in the following form:

$$f(\omega, \vec{e}) = \alpha \omega^2 p(\omega) \sum_{\vec{r}} [\Gamma(\vec{r}) + \Gamma_{sh}(\vec{r}, \vec{e})] e^{i \frac{2\omega}{c} \vec{e} \cdot \vec{r}} \delta \vec{r} + v(\omega, \vec{e}) \quad (1)$$

where $f(\omega, \vec{e})$ represents the measured waveform as a function of frequency ω and direction \vec{e} ; $p(\omega)$ represents the acoustic system response (including the transducer and propagation path); and $v(\omega, \vec{e})$ represents the noise, assumed Gaussian and stationary. Again we assume that the shadow zone is the same for all incident directions. On the basis of this assumption, Eq. (1) can be treated as a

*The even function required can be avoided by a more complex analysis.



SC5391.5FR

problem in classical imaging, in the sense that each measurement (ω, \vec{e}) provides one spatial Fourier component of the scatterer distribution, where the spatial frequency \vec{q} is given by $(2\omega/c)\vec{e}$, and the spatial frequency function $\zeta(\vec{q})$ is $f(\omega, \vec{e})/[\alpha\omega^2 p(\omega)]$. The image $\Gamma(\vec{r})$ is related to $\zeta(\vec{q})$ by

$$\zeta(\vec{q}) = \sum_{\vec{r}} [\Gamma(\vec{r}) + \Gamma_{sh}(\vec{r})] e^{i\vec{q} \cdot \vec{r}} \delta\vec{r} . \quad (2)$$

The image of the object plus shadow zone, $[\Gamma(\vec{r}) + \Gamma_{sh}(\vec{r})]$, thus can be obtained from $\zeta(\vec{q})$ by simple Fourier inversion, provided $\zeta(\vec{q})$ is known at a sufficient number of points in \vec{q} space. To sample the image on a rectangular grid in real space, of dimensions L_x, L_y, L_z at intervals of $\Delta x, \Delta y, \Delta z$, it is necessary to know $\zeta(\vec{q})$ on a corresponding grid in q-space, of dimensions $2\pi/\Delta x, 2\pi/\Delta y, 2\pi/\Delta z$ and intervals of $2\pi/L_x, 2\pi/L_y, 2\pi/L_z$. The image reconstruction technique can be thought of as performing an interpolation of the measured spatial frequencies onto the unmeasured portion of this grid. In the conventional imaging approach, grid cells lying near measured spatial frequencies are set at the mean value within some averaging window, and unsampled cells are set at zero. If the averaging window used is a simple box, the technique is known as box convolution. One noteworthy property of box convolution is that the resulting image $D(\vec{r})$ is related to the true image $[\Gamma(\vec{r}) + \Gamma_{sh}(\vec{r})]$ via a linear operator, representing convolution with the theoretical response to a point scatterer, $B(\vec{r})$. $D(\vec{r})$ and $B(\vec{r})$ are often referred to as the dirty image and synthesized beam respectively. We can then write:

$$D(\vec{r}) = \sum_{\vec{r}'} B(\vec{r} - \vec{r}') \zeta(\vec{r}') + v(\vec{r}) \quad (3)$$

where $\zeta(\vec{r}) = \Gamma(\vec{r}) + \Gamma_{sh}(\vec{r})$, and $v(\vec{r})$ represents the noise resulting from measurement error.

One technique inverting this equation is the CLEAN algorithm. For the purpose of this technique we consider the true image as a series of delta functions, which when convolved with the synthesized beam and linearly superposed, constitute the dirty image. The CLEAN algorithm attempts to determine the



Rockwell International
Science Center

SC5391.5FR

amplitude and location of each of these delta functions. The steps involved in the algorithm starting from the i^{th} iteration, are as follows:

- (1) Locate the peak in $D(\vec{r})$. Let its location be \vec{r}_i and its amplitude be A_i .
- (2) Scale $B(\vec{r})$ by $c_i = \epsilon A_i$ where ϵ is a parameter between 0 and 1 called the "loop gain".
- (3) Subtract $c_i \cdot B(\vec{r} - \vec{r}_i)$ from $D(\vec{r})$, and store c_i, \vec{r}_i .
- (4) Repeat the process from step (1) until the peak of the remaining image is below some preset threshold. Denote this residual image $R(\vec{r})$. We can then express the original dirty image $D(\vec{r})$ as:

$$D(\vec{r}) = \sum_i c_i \cdot B(\vec{r} - \vec{r}_i) + R(\vec{r}) .$$

If we define:

$$I(\vec{r}) = \sum_i c_i \delta(\vec{r} - \vec{r}_i)$$

then $D(\vec{r})$ represents the convolution of $I(\vec{r})$ with $B(\vec{r})$, plus a noise term $R(\vec{r})$. $I(\vec{r})$ thus represents a possible solution for the true image $\zeta(\vec{r})$ on the basis of Eq. (3).

- (5) Form the final "clean" image by convolving $I(\vec{r})$ with a simple function such as a Gaussian whose width is chosen to correspond to the desired spatial resolution, and add this smoothed image to the residual image, $R(\vec{r})$.

The 50% contour of the final "clean" image would provide a reasonable estimate of the boundary of the scatterer.



SC5391.5FR

4.3.4 Elevation Function Algorithm Using the Conjugate Vector Method

A disadvantage of the "CLEAN + thresholding" algorithm is that it is not capable of producing superresolution, i.e. resolution beyond the diffraction limit. On the other hand, the inclusion algorithm achieves a certain degree of super-resolution by making explicit use of the fact that we are dealing with a hard surface. The large amount of computation involved in the 3-dimensional version of this approach, however, has led to consideration of a variant of the algorithm in which the scatterer is represented in terms of a single-valued elevation function. As with the "CLEAN + thresholding" algorithm, we are at present unable to treat the shadow zone exactly. In this case we assume that the shadow zone is nonexistent, i.e. that all parts of the object are visible from all of the incident directions used. Although this situation is physically realizable if the surface to be imaged is sufficiently flat, it is not a situation likely to occur in robotics. However, as with the "CLEAN + thresholding" algorithm, it might still be expected to produce a reasonable image of the illuminated portion of the object. This representation forms the basis of the elevation-function algorithm, and we now discuss the inversion procedure.

In this case, it is more convenient to work in the time domain, and we consider a stochastic measurement model of the form:

$$f(t, \vec{e}) = \frac{\alpha c}{2\vec{e} \cdot \vec{e}_z} \sum_r \delta_r p'(t - 2c^{-1}\vec{e} \cdot \vec{r} - 2c^{-1}\vec{e} \cdot \vec{e}_z Z(r)) + v(t, \vec{e}) \quad (1)$$

where $Z(\underline{r})$ represents the elevation function at location \underline{r} (in the xy-plane); δ_r is the area of a pixel; and f , p , and v are as defined in Section 4.2. The vector \underline{r} takes values on a 2-d grid in the xy-plane (in contrast to \vec{r} in Eq. (1) of the previous section, which is 3-dimensional) extending over a specified localization area outside of which $Z(\underline{r})$ is known to vanish. The function $Z(\underline{r})$ is assumed to be random a priori and statistically independent of $v(t, \vec{e})$. We also assume that $Z(\underline{r})$ and $Z(\underline{r}')$ are statistically independent when $\underline{r} \neq \underline{r}'$. The a priori probability density of $Z(\underline{r})$ at a single point \underline{r} will be assumed to be a specified function $P(Z(\underline{r}))$ having a form independent of \underline{r} for all \underline{r} in the localization domain.



Rockwell International
Science Center

SC5391.5FR

The problem of determining the most probable elevation function $Z(\underline{r})$ given the measurements $f(t, \vec{e})$ involves the maximization of the expression

$$\begin{aligned} \ln P(\Gamma, f) = & -\frac{1}{2\sigma_v^2} \sum_{t, \vec{e}} [f(t, \vec{e}) - \frac{\alpha c}{2\vec{e} \cdot \vec{e}_z} \sum_r \delta_r p'(t - 2c^{-1}\vec{e} \cdot \underline{r} - 2c^{-1}\vec{e} \cdot \vec{e}_z Z(\underline{r}))]^2 \\ & + \sum_r \ln P(Z(\underline{r})) \end{aligned} \quad (2)$$

with respect to $Z(\underline{r})$. Using the conjugate vector method we are led to consider the function

$$\begin{aligned} \psi(\Gamma, w, f) = & \sum_{t, \vec{e}} \frac{1}{2} \sigma_v^2 w(t, \vec{e})^2 - w(t, \vec{e}) f(t, \vec{e}) \\ & + \sum_r \phi(w, Z(\underline{r}), \underline{r}) + \ln P(Z(\underline{r})) \end{aligned} \quad (3)$$

where

$$\phi(w, Z(\underline{r}), \underline{r}) = \delta_r \sum_{t, \vec{e}} w(t, \vec{e}) \frac{\alpha c}{2\vec{e} \cdot \vec{e}_z} p'(t - 2c^{-1}\vec{e} \cdot \underline{r} - 2c^{-1}\vec{e} \cdot \vec{e}_z Z(\underline{r})) \quad (4)$$

If ψ is minimized on w , then the original function defined by Eq. (2) is recovered. However, if ψ is first maximized on Z and then minimized on w (assuming that the reversal of the order of minimization on w and maximization on Z is valid), then one is led down an entirely different path. Explicitly we consider the minimization of $\chi(w, f)$ on w where χ is defined by

$$\chi(w, f) = \sum_{t, \vec{e}} \frac{1}{2} \sigma_v^2 w(t, \vec{e})^2 - w(t, \vec{e}) f(t, \vec{e}) + \sum_r g(w, \underline{r}) \quad (5)$$

in which

$$g(w, \underline{r}) = \max_{Z(\underline{r})} \phi(w, Z(\underline{r}), \underline{r}) + \ln P(Z(\underline{r})).$$



SC5391.5FR

χ is readily shown to be a convex function of w , and hence the minimization can be accomplished by a standard gradient method. The maximization on $Z(r)$ has to be done by direct search, although this does not represent a significant computational problem since the maximization involves only a 1-dimensional search, and is conducted independently for each pixel.

4.3.5 Results Based Upon Synthetic and Experimental Test Waveforms

Prior to the start of this program, we had made some preliminary tests with the inclusion algorithm using synthetic data. The results are reported by Marsh and Richardson (1983). Briefly, our goal was to investigate the fidelity of reconstruction of a hard spherical scatterer in air, using synthetic measurements consisting of three incident directions (and also three oppositely-directed pairs of measurements). In generating the synthetic data we actually used the impulse response for a void in a solid. As with a solid object in air, a large impedance discontinuity is involved, so the results should be very similar, except for the change in sign which was taken into account. The incident directions used (in terms of the polar and azimuthal angles θ and ϕ defined in Fig. 3) were $\theta = 54.7^\circ$; $\phi = 0^\circ$, 120° and 240° . The transducer response was in the shape of a Hanning window in the frequency domain, covering the frequency range corresponding to $ka = 0$ to 3.66 (between the zero points of the window). The sphere was assumed to be at the origin of the coordinate system. The reconstructed elevation profile above a base plane passing through the center of the spheres is shown in Fig. 7, represented as a hidden-line surface with a field of view of twice the diameter of the assumed sphere.

Various artifacts in the reconstruction are probably due to errors in the Kirchhoff approximation; but there may also be a contribution from a problem with this particular application of the conjugate-vector method, the nature of which is now understood, and is discussed in Richardson and Marsh (1983c).

In the DARPA-funded program, tests were run using both synthetic and experimental data for the "CLEAN + thresholding" algorithm and the elevation-function algorithm. We now discuss the results.



SC5391.5FR

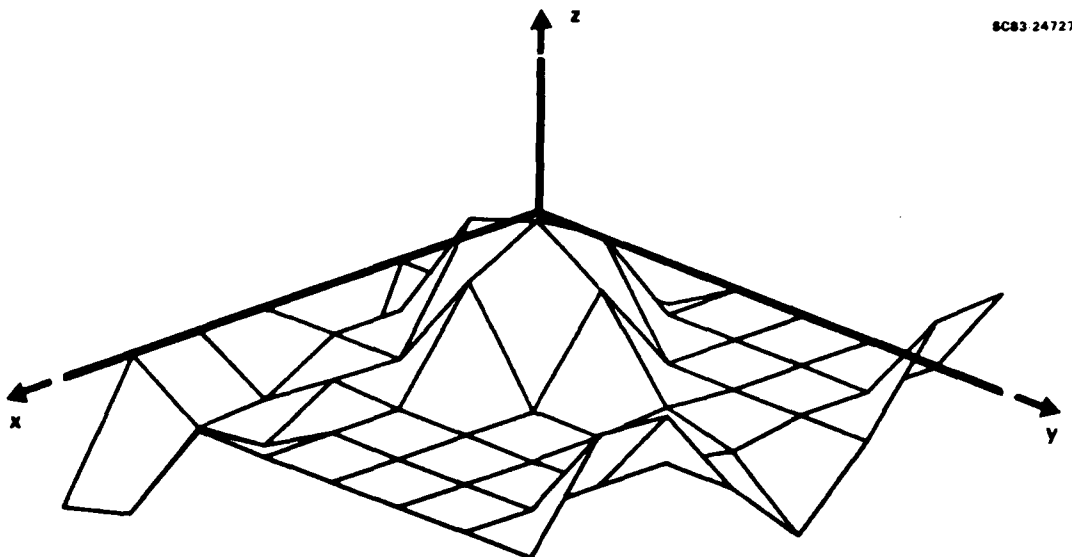


Fig. 7 Elevation profile reconstructed from three incident directions using the inclusion algorithm.

Both algorithms were tested with synthetic data for a sphere. The reference waveforms corresponded to a set of transducers whose frequency range covered the ka range 0.6 - 1.8, where a is the radius of the sphere, and k is the wavenumber. The response was in the shape of a Hanning window. For a sphere of diameter 1 cm in air, the corresponding frequency range would be 6.6 - 19.8 kHz. Data were generated for a set of 4 incident angles, corresponding to the 3 corners of a cube, plus the body diagonal, the latter defined to be the z axis. In terms of the coordinate system defined in Fig. 3, the directions were:

- (1) $\theta = 54.7^\circ$, $\phi = 0^\circ$
- (2) $\theta = 54.7^\circ$, $\phi = 120^\circ$
- (3) $\theta = 54.7^\circ$, $\phi = 240^\circ$
- (4) $\theta = 0^\circ$

In generating these data, we actually used the impulse response for a void in a solid, as before.



SC5391.5FR

The results for the two algorithms are presented in Fig. 8 in the form of hidden-line representations as before. Satisfactory reconstructions were obtained in both cases, except for the pair of spurious peaks in the second algorithm. These peaks are probably due to errors in the Kirchhoff approximation. The errors in deduced radius (from the vertical extent of each plot) were + 1% and -12.5% for the two algorithms, respectively.

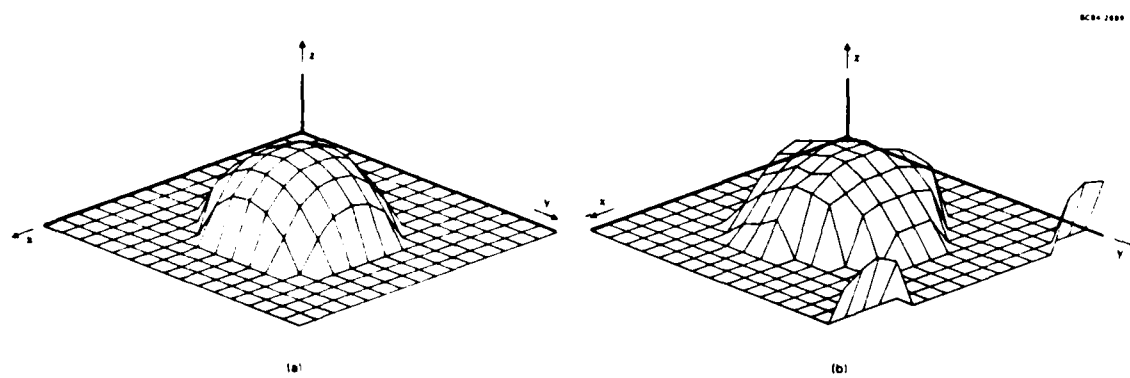


Fig. 8 Reconstruction of the surface of a sphere from synthetic data, using (a) the "CLEAN + thresholding" algorithm, and (b) the elevation function algorithm.

We now discuss the experiments which were designed to obtain pulse-echo scattering data in air from isolated small objects of dimensions ~ 1 cm. A convenient type of transducer for this purpose was fabricated from a piezoelectric polymer, and with the appropriate electronics, it provided an operating bandwidth of 7 - 16 kHz at the 10% level. A closely spaced pair of such transducers was used, one for sending and one for receiving, providing a good approximation to a pulse-echo setup. The scatterer was hung from the ceiling with a thin thread. The same set of four incident directions was used as for the synthetic data, and were defined in the previous section. These incident directions were provided by attaching the transducer pair to a PUMA 560 robot arm, and by positioning the arm sequentially in the four positions with respect to the hanging object. The position repeatability of this robot approximates 0.01 cm, an error that is a satisfactorily small fraction of a typical wavelength (~ 3 cm). The



SC5391.5FR

received waveform was digitized with eight bits of amplitude quantization with a time sampling rate of 25 MHz, considerably finer than actually required. After digitization, the waveform was passed to a VAX 11/780 for processing.

The objects were a metal sphere of diameter 1.25 cm, and a plastic tetrahedron with sides of length 2 cm. The tetrahedron was oriented such that one of the flat surfaces was in the xy-plane, and the apex was towards the transducer for the vertical incident direction. We wanted to measure the reference waveform (measurement system response function) $p_n(t)$ for the n^{th} incident direction by means of measurements of a smaller sphere 0.475 cm in diameter, comfortably in the Rayleigh scattering regime, and therefore with a known theoretical response. The scattering amplitude for the pulse-echo mode is, in fact, given by:

$$A(\omega) = \frac{2}{3} \left(\frac{\omega}{c} \right)^2 a^3 \quad (3)$$

where a is the radius of the scatterer.

In practice, the response of the small sphere was insufficient to enable a satisfactory calibration; hence an indirect procedure was necessary. The shape of $p_n(t)$ was measured accurately by means of the reflection from a flat plate, except for an unknown time shift and vertical scaling factor. The latter quantity was obtained from the measurements of the small sphere (using the one good waveform obtained), and the time shifts were obtained from the waveforms of the large sphere. For this reason, the center of the large sphere defines the spatial origin for the entire experiment. The reference waveform together with a sample waveform from the large sphere is shown in Fig. 9. Image reconstruction was performed using the CLEAN + thresholding algorithm.

Figure 10a shows a hidden-line representation of the image of the sphere. The reconstructed shape is satisfactorily spherical, and the inferred diameter, 1.2 cm, is very close to the true value of 1.25 cm. Note that since the sphere waveforms were used to obtain the time delays for obtaining $p_n(t)$, the center of the sphere defines our spatial origin, and the image contains no information on the absolute spatial location of the sphere.



Rockwell International
Science Center

SC5391.5FR

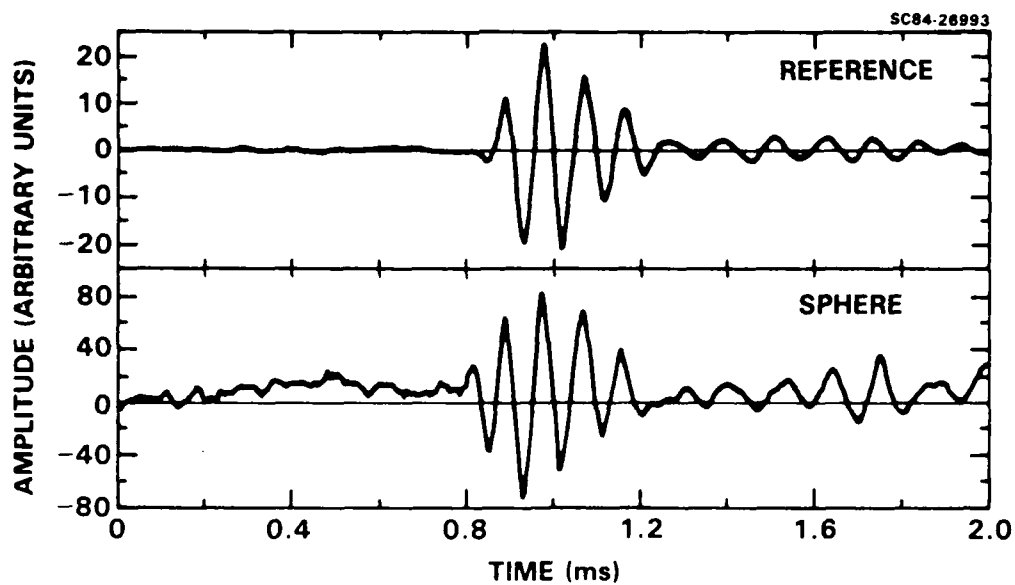


Fig. 9 Experimental waveforms.

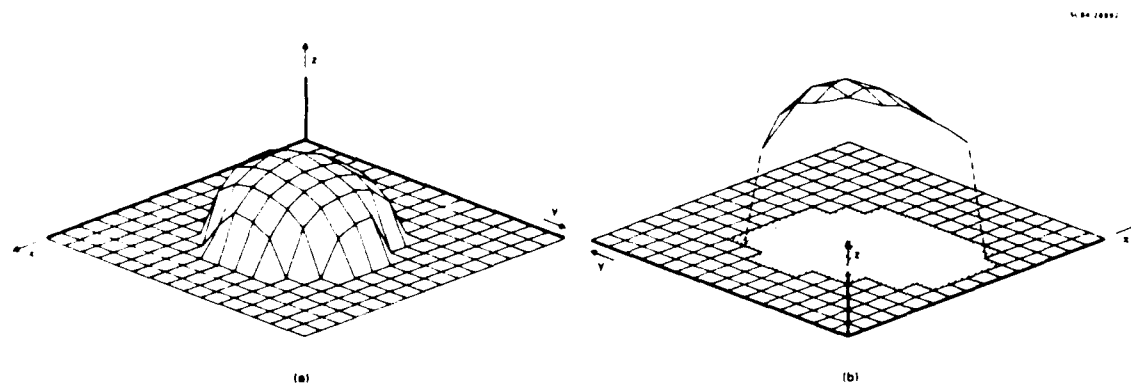


Fig. 10 Reconstruction from experimental data.



SC5391.5FR

4.4.5 Two Computational Examples With an Unsymmetrical Transducer Configuration

In this section we consider a second computational example that differs from the last one in only one essential respect, namely that an unsymmetrical set of incident directions has been selected. These results represent an advance over those given in the last section. The basis of this advance rests upon some recently discovered ambiguity theorems to be discussed later. The scope of our investigation was limited as before to flat-bottomed rigid objects represented by single-valued elevation functions. The scope was further limited to elevation functions with fairly gentle slopes and to situations in which acoustical shadows either do not exist or can be neglected.

As usual the best estimate is the vector Z that maximizes the conditional probability $P(Z|f)$ where $Z = Z(\underline{r})$ is the set of elevations at points \underline{r} in the xy -plane on an appropriate grid bounded by the assumed localization domain and where $f = f(t,e)$ is the set of measured amplitudes at a discrete set of times t and incident directions \vec{e} . As in the last section the a priori statistical properties of the elevation function $Z(\underline{r})$ and the measurement error $v(t,e)$ were both assumed to be Gaussian with zero means and diagonal covariance matrices. In the case of the elevation function, assuming a priori statistics that involve an additional positivity constraint is preferable. However, the simpler pure Gaussian model simplifies the solution by enabling exact linear estimation procedures to be used at each step of the iteration process described later.

Additional ambiguity theorems that must be considered in choosing the experimental set-up, real or hypothetical have been discovered recently (see Section 4.5). An ambiguity theorem deals with a statement like "A measurement system M gives the same results for objects A and B." As we will discuss more fully later, we have discovered that any measurement system with n-fold rotational symmetry (e.g., the three-fold symmetry obtained when $-\vec{e} = (100), (010),$ and (001) with (111) parallel to the z-axis) can encounter certain pairs of objects (or the same object in two orientations) that give the same measured results. Thus, when the a priori probabilities are the same, the imaging algo-



Rockwell International
Science Center

SC5391.5FR

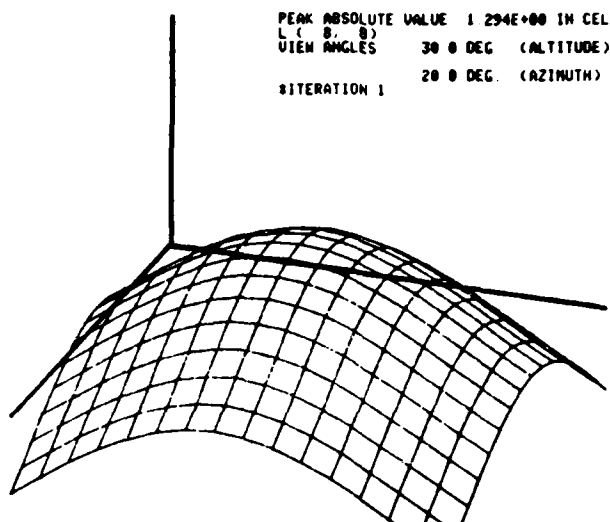


Fig. 13 Estimated elevation function for iteration #1.

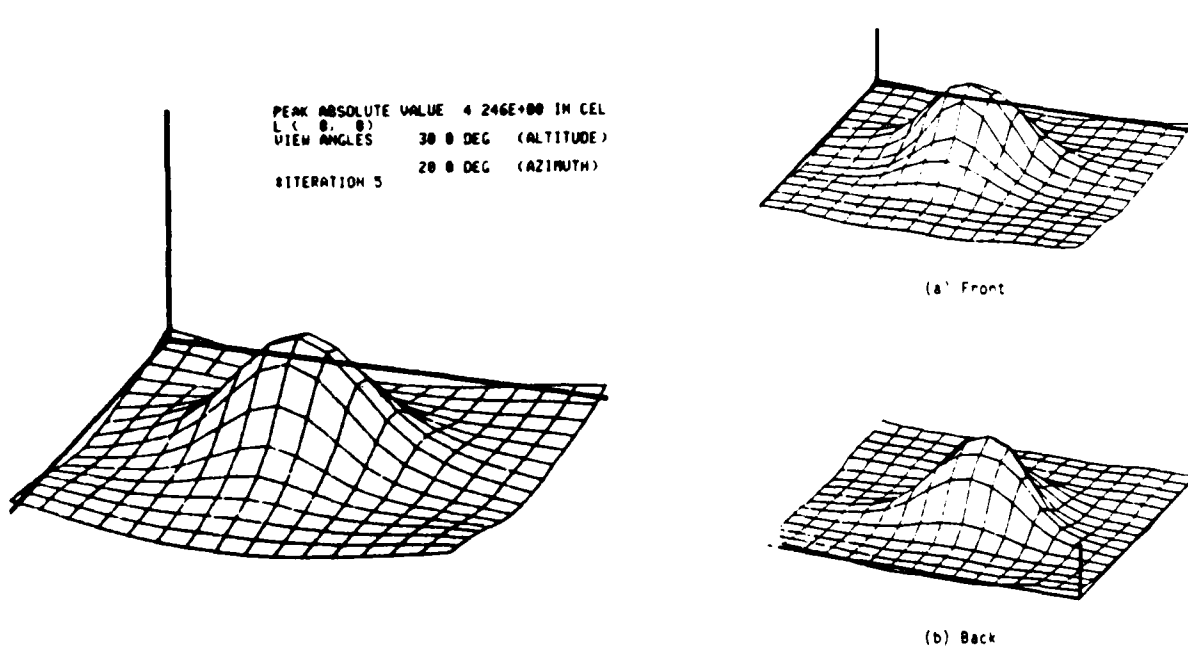


Fig. 14 Estimated elevation function for iteration #5.

Fig. 15 Estimated elevation function for iteration #8.



SC5391.5FR

Table 1
Estimation Parameters

Iteration No.	ω_{\max} (kHz)	$f(t, \vec{e})_{\max} / \sigma_v$
1	10	10
2	10	10
3	10	10
4	20	10
5	30	10
6	30	10
7	40	10
8	40	33

another. In the iterations we will specify the various values of ω_{\max} assumed, but we will take a fixed value of $\omega_{\min} = 1$ kHz.

In Figs. 13 and 14 we show the stages of development of the estimated elevation function corresponding to iterations #1 and #5 (see Table 1). Clearly a significant improvement in resolution is achieved in the first four iterations. Finally, in Figs. 15a and 15b we show the front and back views, respectively, of the estimated elevation function at the last iteration, i.e., #8, in our imaging procedure. The final estimated elevation function is a smoothed version of the elevation function of the true squashed tetrahedron illustrated in Fig. 12. The degree of smoothing, according to rough calculations, appears to be consistent with the Hanning window with $\omega_{\max} = 40$ kHz. We expect a certain amount of super-resolution to be present, but this is difficult to prove on the basis of the present results. However, a significant amount of implicit k-space interpolation is present.



Rockwell International
Science Center

SC5391.5FR

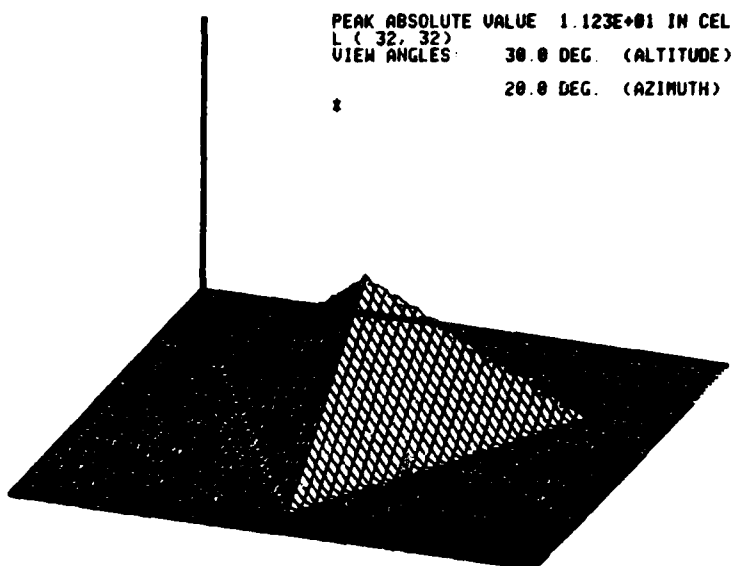


Fig. 12 Assumed squashed tetrahedron.

The constant α will be taken equal to 1 since its common value occurs in both the preparation of synthetic test data and the imaging algorithm and thus can be regarded as self-cancelling. The velocity of sound in air, c , is assumed to be $345 \text{ m s}^{-1} = 0.345 \text{ mm } (\mu\text{s})^{-1}$. We will use a signal-to-noise ratio η defined by

$$\eta = \tilde{f}(t, \vec{e})_{\max} / \sigma_v \quad (2)$$

where $\tilde{f}(t, \vec{e})_{\max}$ is the maximum (with respect to t and e) of the waveform corresponding to noiseless synthetic test data and where σ_v is the standard deviation of $v(t, \vec{e})$. The function $p(t)$ is given in the frequency domain by a Hanning window between the frequency limits ω_{\min} and ω_{\max} .

In Table 1 below we list the sequence of parameter values used in the present example of the iterative solution. Here we will assume that the low-pass filtering operation (corresponding to the time-domain convolution of $H_m(t)$ with $p(t)$) is approximately equivalent to changing one Hanning window into



Rockwell International

Science Center

SC5391.5FR

to a suitable criterion. At the present time we have not established a procedure for selecting the sequence of transfer functions $H_m(t)$; thus, this selection remains a problem to be handled by computer experimentation. We have also tried varying other parameters (e.g., σ_v) during the iteration process.

4.4.4 A Computational Example With a Symmetrical Transducer Configuration

In this section we present an example of the above iterative approach using synthetic test data. The main purpose of this computation is to provide some insight into what imaging performance is possible with a relatively sparse set of scattering measurements in the absence of scattering theory errors and measurement error. The first type of error is avoided by using the same Kirchhoff approximation in both the preparation of synthetic data and the imaging procedure; however, even in the case of real test data a major part of the Kirchhoff error is avoided by limiting our treatment to cases in which acoustical shadowing does not exist. The second type of error, i.e., that due to imperfect measurement, is avoided by setting $\sigma_v = 0$ in the preparation of test data; we must emphasize, however, that in the imaging procedure σ_v is assigned various positive values, a matter that will be discussed later in greater detail.

In the production of synthetic test data we assume that the object of interest is a squashed tetrahedron, i.e., a regular tetrahedron with its vertical scale reduced by a factor of two. In particular, we have a tetrahedron with horizontal edges having a common length of 13.75 mm and with a height of 5.61 mm, as shown in Fig. 12. In this example we have assumed a set of five pulse echo measurements (one more than the hypothesized minimal number) each with an incident direction defined by

$$\vec{e} = -(\vec{e}_x \cos \phi + \vec{e}_y \sin \phi) \sin \theta - \vec{e}_z \cos \theta \quad (1)$$

and given by the value of azimuthal and polar angles, ϕ and θ , respectively, tabulated below

$$\begin{array}{ccccc} \theta & = & 0 & 54.7^\circ & 54.7^\circ & 54.7^\circ & , \\ \phi & = & - & 0^\circ & 90^\circ & 180^\circ & 270^\circ . \end{array}$$



SC5391.5FR

Let us denote the best estimate for the m th stage by $\hat{z}_m(\underline{r})$. It is given by an expression similar to (2) except for several important differences as can be seen in the following equation

$$\begin{aligned}\hat{z}_m(\underline{r}) = & \sigma_z^2 \delta_r \alpha \sum_{t, \vec{e}} \sum_{t', \vec{e}'} p_m''(t - 2c^{-1}\vec{e} \cdot \underline{r} \\ & - 2c^{-1}\vec{e} \cdot \vec{e}_z \hat{z}_{m-1}(\underline{r})) \cdot C_{fm}(t, \vec{e}; t', \vec{e}')^{-1} g_m(t', \vec{e}') ,\end{aligned}\quad (9)$$

where $C_{fm}(t, \vec{e}; t', \vec{e}')^{-1}$ is the matrix inverse of

$$\begin{aligned}C_{fm}(t, \vec{e}; t', \vec{e}') = & \sigma_z^2 \delta_r \alpha^2 \sum_r \delta_r p''(t - 2c^{-1}\vec{e} \cdot \underline{r} - 2c^{-1}\vec{e} \cdot \vec{e}_z \hat{z}_{m-1}(\underline{r})) \\ & \cdot p''(t' - 2c^{-1}\vec{e}' \cdot \underline{r} - 2c^{-1}\vec{e}' \cdot \vec{e}_z \hat{z}_{m-1}(\underline{r})) + \delta_{tt'} \delta_{\vec{e}\vec{e}'} \sigma_v^2 ,\end{aligned}\quad (10)$$

and where $g_m(t, \vec{e})$ is defined by (7).

The next step in the recursive procedure is to select a time-domain transfer function $H_{m+1}(t)$ corresponding to a higher frequency roll-off in the low-pass filter (this represents an incremental unsmoothing of the previously smoothed $f(t, e)$ and $p(t)$). We then use $Z_m(\underline{r})$ as a new point in state space about which the measurement model is to be linearized. We then obtain eventually a new estimate $Z_{m+1}(\underline{r})$ given by (7), (9) and (10) with the subscript m replaced by $m+1$.

The total recursion procedure is straightforward, at least in principle. We commence with $Z_0(\underline{r}) = 0$, or some other initial estimate (e.g., the result of the "CLEAN + thresholding" algorithm), and a choice of $H_1(t)$ such that the characteristic wavelengths involved in the smoothed version of $f(t, \vec{e})$ and $p(t)$ are sufficiently long. The recursion process is carried on until the difference between successive approximations becomes sufficiently small according



SC5391.5FR

$$\begin{aligned} f_m(t, \vec{e}) = & -\frac{\alpha c}{2\vec{e} \cdot \vec{e}_z} \sum_r \delta_r [p_m'(t - 2c^{-1}\vec{e} \cdot \underline{r} \\ & - 2c^{-1}\vec{e} \cdot \vec{e}_z \hat{z}_{m-1}(r)) - p_m'(t - 2c^{-1}\vec{e} \cdot \underline{r})] \\ & + \alpha \sum_r \delta_r p_m''[t - 2c^{-1}\vec{e} \cdot \underline{r} - 2c^{-1}\vec{e} \cdot \vec{e}_z \hat{z}_{m-1}(r)] \\ & \cdot [Z(r) - \hat{z}_{m-1}(r)] + v(t, \vec{e}) \quad . \end{aligned} \quad (6)$$

Defining the new function

$$\begin{aligned} g_m(t, \vec{e}) \triangleq & f_m(t, \vec{e}) + \frac{\alpha c}{2\vec{e} \cdot \vec{e}_z} \sum_r \delta_r [p_m'(t - 2c^{-1}\vec{e} \cdot \underline{r} \\ & - 2c^{-1}\vec{e} \cdot \vec{e}_z \hat{z}_{m-1}(r)) - p_m'(t - 2c^{-1}\vec{e} \cdot \underline{r})] \\ & + \alpha \sum_r \delta_r p_m''(t - 2c^{-1}\vec{e} \cdot \underline{r} - 2c^{-1}\vec{e} \cdot \vec{e}_z \hat{z}_{m-1}(r)) \hat{z}_{m-1}(r) \quad , \end{aligned} \quad (7)$$

we can rewrite (6) in the simpler form

$$\begin{aligned} g_m(t, \vec{e}) = & \alpha \sum_r \delta_r p_m''(t - 2c^{-1}\vec{e} \cdot \underline{r} \\ & - 2c^{-1}\vec{e} \cdot \vec{e}_z \hat{z}_{m-1}(r)) Z(r) + v(t, \vec{e}) \end{aligned} \quad (8)$$

In this model $Z(r)$ and $v(t, \vec{e})$ have the same a priori statistical properties as before, i.e., the entities are Gaussian random vectors with properties given by (2a) - (4), inclusive.



SC5391.5FR

If the grid in the xy -plane is regarded as having a uniform but variable (from case to case) mesh size, then σ_z^2 should be inversely proportional to δr if $Z(r)$ is spatially white (a priori) in the continuous case. Clearly then, (2) and (3) approach the proper continuous limits as $\delta r \rightarrow 0$. Another point worth noting is that in (2) the function $f(t, \vec{e})$ should be replaced by the set of actually measured values when the estimate is based on measurements.

These results suggest an iterative method for the general case. As we have already indicated, the basic idea is to use a linearization with respect to the incremental correction in $Z(r)$ combined with a low-pass filtering operation applied to $f(t, \vec{e})$ and $p(t)$, but not to $v(t, \vec{e})$, in order to make the linearization valid. In more explicit mathematical terms, we assume that the filtered versions of $f(t, \vec{e})$ and $p(t)$ are given by

$$f_m(t, \vec{e}) = H_m(t) * f(t, \vec{e}) , \quad (4a)$$

$$p_m(t) = H_m(t) * p(t) , \quad (4b)$$

where $*$ denotes temporal convolution and $H_m(t)$ is the time-domain transfer function representing the low-pass filter associated with the m th stage. The exact model for the filtered measurement process for the m th stage is clearly given by

$$\begin{aligned} f_m(t, \vec{e}) = & - \frac{\alpha c}{2\vec{e} \cdot \vec{e}_z} \sum_r \delta r [p'_m(t - 2c^{-1}\vec{e} \cdot \underline{r} \\ & - 2c^{-1}\vec{e} \cdot \vec{e}_z Z(r)) - p'_m(t - 2c^{-1}\vec{e} \cdot \underline{r})] \\ & + v(t, \vec{e}) . \end{aligned} \quad (5)$$

Let us now linearize the above expression with respect to the difference between $Z(r)$ and the best estimate $\hat{Z}_{m-1}(r)$ associated with the previous stage. We obtain



SC5391.5FR

In the present section we discuss a new method for dealing with the above problem. This method involves a recursive procedure in which $f(t, \vec{e})$ and $p'(t)$ are initially subjected to a common smoothing operation that has the property that the smoothed version of $p'[t - 2c^{-1}\vec{e} \cdot \underline{r} - 2c^{-1}\vec{e} \cdot \vec{e}_z Z(\underline{r})]$ can be linearized with respect to $Z(\underline{r})$. Later stages of the procedure involve successive unsmoothing and linearizations with respect to incremental corrections to $Z(\underline{r})$.

First we consider the case in which the characteristic wavelength involved in $p(t)$ is large compared with a characteristic elevation function Z^* , e.g., the a priori m.s. value of $Z(\underline{r})$. This means that $p'(t)$ can be regarded as linear to a sufficient level of accuracy in any time interval of length $2c^{-1}\vec{e} \cdot \vec{e}_z Z^*$. Thus, we can expand the function on the righthand side of Eq. (1) in Section 4.4.2 in a power series in $Z(\underline{r})$, omitting second and higher power terms, with the result

$$f(t, \vec{e}) = \alpha \sum_{\underline{r}} \delta_r p''(t - 2c^{-1}\vec{e} \cdot \underline{r}) Z(\underline{r}) + v(t, \vec{e}) \quad . \quad (1)$$

This is a linear model with Gaussian statistics, a case in which the optimal estimate (i.e., the most probable value given the measurement) is well known. It is given by the expression

$$\hat{Z}(\underline{r}) = \sigma_z^2 \delta_r \alpha \sum_{t, \vec{e}} \sum_{t', \vec{e}'} p''(t - 2c^{-1}\vec{e} \cdot \underline{r}) \cdot C_f(t, \vec{e}; t', \vec{e}')^{-1} f(t', \vec{e}') \quad , \quad (2)$$

where $C_f(t, \vec{e}; t', \vec{e}')^{-1}$ is the matrix inverse of

$$C_f(t, \vec{e}; t', \vec{e}') = \sigma_z^2 \delta_r \alpha^2 \sum_{\underline{r}} \delta_r p''(t - 2c^{-1}\vec{e} \cdot \underline{r}) \cdot p''(t' - 2c^{-1}\vec{e}' \cdot \underline{r}) + \delta_{tt'} \delta_{\vec{e}\vec{e}'} \sigma_v^2 \quad . \quad (3)$$



SC5391.5FR

where $f(t, \vec{e})$, $v(t, \vec{e})$, $p(t)$, α , and c were defined in Section 4.2. The additional symbols \underline{r} , $Z(\underline{r})$, and \vec{e}_z were defined in Section 4.3.4. As before, the time t is assumed to take a discrete set of values corresponding to an appropriate sampling rate over a specified observation interval. The localization domain D_L is defined by the inequalities: $-1/2 L < x < 1/2 L$ and $-1/2 L < y < 1/2 L$.

To give a complete description of the measurement model we must specify the a priori statistics of $Z(\underline{r})$ and $v(t, \vec{e})$. Here we assume that both entities are Gaussian random vectors with the properties

$$EZ(\underline{r}) = 0 \quad , \quad (2a)$$

$$EZ(\underline{r})Z(\underline{r}') = \delta_{\underline{r}\underline{r}'} \sigma_Z^2 \quad , \quad (2b)$$

$$Ev(t, \vec{e}) = 0 \quad , \quad (3a)$$

$$Ev(t, \vec{e})v(t', \vec{e}') = \delta_{tt'} \delta_{\vec{e}\vec{e}'} \sigma_v^2 \quad , \quad (3b)$$

$$EZ(\underline{r})v(t, \vec{e}) = 0 \quad . \quad (4)$$

In (2b) and (2b) the Kronecker deltas, $\delta_{\underline{r}\underline{r}'}$, $\delta_{tt'}$, and $\delta_{\vec{e}\vec{e}'}$, are generalized in an obvious way to the case of noninteger and, in some cases, nonscalar subscripts. $Z(\underline{r})$ is assumed to have a positivity constraint. However, in order to focus exclusively on the problems ensuing from the nonlinear dependence upon $Z(\underline{r})$ in the measurement model (2.1), we defer this case to a later time.

4.4.3 Application of Iterative Method

The determination of the most probable elevation function given the results of scattering measurements, i.e., the determination of $Z(\underline{r})$ that maximizes $P(Z|f)$, cannot be carried out by purely analytical means because of the nonlinear dependence upon $Z(\underline{r})$ in the measurement model (1) in Section 4.4.2. Even though Z and v are Gaussian, a priori, the nonlinearity is a major source of difficulty. An approach that has been tried in the past is discussed in Section 4.3.4.



4.4 Discussion of the Fourth Imaging Algorithm

4.4.1 Comments

At this point we present a few remarks about the relations between the fourth imaging algorithm to be discussed in the following sections and the third imaging algorithm that was discussed in Section 4.3.4. Actually, the two algorithms are based upon essentially identical measurement models. A minor difference is because in the fourth algorithm we redefined the concept of incident wave so that here the measured waveform is the perturbation due to the presence of the object.

The main difference is that here we used a different solution method; namely, an iterative method described in detail below instead of the conjugate vector method. Conceivably, some future improvements in the latter, or the execution of it, may make the third algorithm better than the fourth.

4.4.2 Formulation of the Measurement Model

We assume that an unknown solid object rests upon a reflective table within a known localization domain. A set of pulse-echo scattering measurements is made under conditions such that, as stated before, the localization domain and each transducer are in the far-field of each other. We will define the incident wave to be the wave that would exist in the absence of the object and the scattered wave as the increment due to the presence of the object.

In formulating the measurement model we limit our investigation, as in the case of third imaging algorithm, to objects described by single-valued elevation functions. We limit our discussion to situations in which acoustical shadows either cannot occur or can be neglected.

The appropriate measurement model is represented by the following expression

$$f(t, \vec{e}) = -\frac{\alpha c}{2\vec{e} \cdot \vec{e}_z} \sum_{\underline{r}} \delta_{\underline{r}} [p'(t - 2c^{-1}\vec{e} \cdot \underline{r} - 2c^{-1}\vec{e} \cdot \vec{e}_z Z(\underline{r})) - p'(t - 2c^{-1}\vec{e} \cdot \underline{r})] + v(t, \vec{e}), \quad (1)$$



SC5391.5FR

3. While satisfactory images sometimes could be produced with as few as four incident directions, 15 incident directions were required to ensure good image fidelity in general. However, these diversity requirements were expected to be relaxed somewhat when proper a priori information is taken into account.

Figure 11 shows the results for the hemisphere, tetrahedron, and cube using a measurement system involving 15 incident directions together with a transducer bandwidth of 1.8 - 27 kHz, corresponding to a ka range of 0.5 - 7.5. The 15 incident directions involved polar angles of 0, 25, 50 and 75 degrees, with azimuthal angles evenly spaced in each case. Two hidden-line views of the deduced surface are presented for each object, the viewing directions being indicated in the caption.

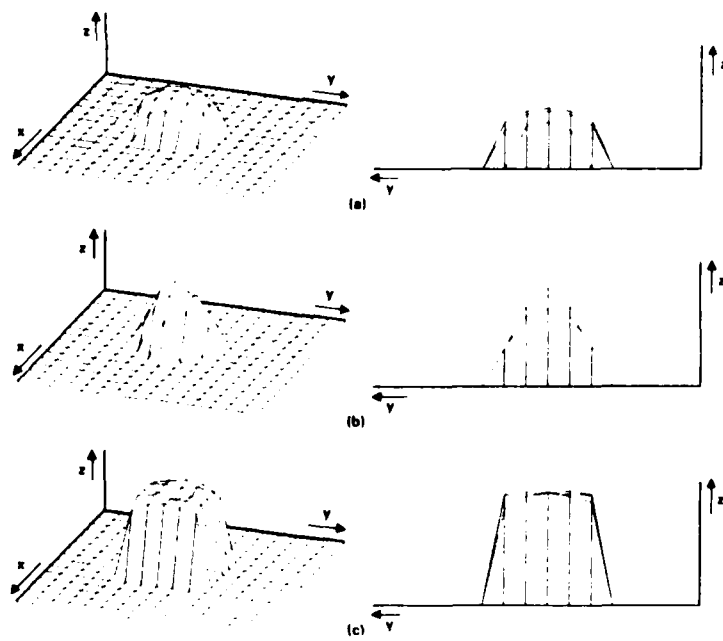


Fig. 11 Inversion results for (a) hemisphere, (b) tetrahedron, and (c) cube using the "CLEAN + thresholding" algorithm. Two hidden-line views of the surface are presented in each case, the one on the left corresponding to elevation and azimuth of 30 and 160 degrees respectively, and the one on the right corresponding to zero elevation and azimuth.



SC5391.5FR

corresponding to the transducer response, using various assumed bandwidths. In generating the synthetic data, the same approximations (see Section 4.2) were made as in the previous tests; namely, neglect of shadows and multiple reflections. With regard to the former, experience with inverting exact synthetic data for an isolated sphere leads us to believe that this would not have a serious effect on the deduced shape of the illuminated portion of the object. In the case of the latter, the effects of multiple reflections in most cases would be felt at sufficiently late times that the imaging algorithm would interpret them as due to spurious scatterers in the interior of the object.

The first step in the inversion procedure was to subtract the "table only" waveform from the "object + table" waveform in each case. The measurement model used in the inversion algorithm was appropriate for dealing with these subtracted waveforms. Image reconstruction was then performed using the "CLEAN + thresholding algorithm," in the usual manner. The final thresholding step, used to estimate the boundary of the object, was performed at the 40% level.

The above procedure was carried out for a variety of measurement systems, for the hemisphere, tetrahedron, and cube. In each case, an elevation profile was deduced and was presented on a square hidden-line surface plot of size 16×16 pixels, corresponding to a field of view of 8 cm. The following general conclusions emerged:

1. In order to define the global structure of the objects, measurements below a frequency corresponding to $ka = 1$ were required, where k is the wavenumber and $a = L/2$.
2. To obtain sufficient spatial resolution to define key features of the shape of the object, frequencies as high as $ka = 7.5$ were required. This is consistent with our expectations, given that CLEAN produces no superresolution, and is limited by diffraction to a resolution of $c/(4f[\max])$ where c is the speed of sound, and $f[\max]$ is the maximum measured frequency.



SC5391.5FR

In the case of the tetrahedron (Fig. 10b) the imaging algorithm has produced a surface whose base area is similar to that of the original object but whose vertical extent is smaller by a factor of 2. The appearance is significantly non-spherical, and is consistent with a severe spatial smoothing of the original object. Since CLEAN does not provide superresolution, this behavior was not unexpected. The vertical displacement of the imaged surface above the base plane almost certainly represents the true physical displacement of the tetrahedron from the sphere. The fact that only the upper surface of the object has been imaged is a consequence of the Kirchhoff approximation in which the rest of the object is considered to be in the shadow zone.

We conclude that the results of imaging the sphere with experimental data using the "CLEAN + thresholding" algorithm gave satisfactory results. In the case of the tetrahedron, however, the spatial resolution was insufficient for a proper characterization of the object.

The situation would be expected to improve with the use of the elevation-function algorithm owing to the super-resolution capability arising from the a priori information embedded in the algorithm for this case, and further developments and testing of this algorithm will be discussed in Section 4.4. In the meantime, we explored further the behavior of the "CLEAN + thresholding" algorithm in regard to the bandwidth and number of incident directions required to reconstruct objects of various shapes. We now discuss these results.

The objects selected for these tests were a hemisphere, tetrahedron, and a cube, each of which was assumed to be sitting on a flat, perfectly reflective table. The characteristic dimension, L, for each object was taken to be 3 cm, where L represents the diameter in the case of the hemisphere, and height in the case of the tetrahedron and cube. Data were synthetically generated on the basis of the Kirchhoff approximation for a series of incident directions, each characterized by a polar angle θ and azimuthal angle ϕ , as defined in Fig. 4, the z-axis taken to be perpendicular to the surface of the table. In addition to the sets of waveforms for each object sitting on the table, a set of waveforms was also generated corresponding to measurements of the table in the absence of an object. Data were also generated for the reference waveform,



Rockwell International

Science Center

SC5391.5FR

rithms cannot determine which member of a pair is most probable. For this reason we have selected a set of transducer positions and orientations corresponding to an unsymmetrical set of incident directions. In particular, we have selected a set of incident directions defined by

$$-\vec{e} = (\vec{e}_x \cos \theta + \vec{e}_y \sin \phi) \sin \theta + \vec{e}_z \cos \theta$$

and corresponding to the polar and azimuthal angles, θ and ϕ , respectively, tabulated below

$\theta = 0^\circ$	54.7°	54.7°	54.7°	54.7°
$\phi = -$	0°	90°	135°	225°

The corresponding transducer configuration is illustrated in Fig. 16. This selection of directions avoids the ambiguities associated with four-fold symmetry, but does not avoid ambiguities associated with eight-fold symmetry as we will see in the later, more detailed, discussion of ambiguity theorems.

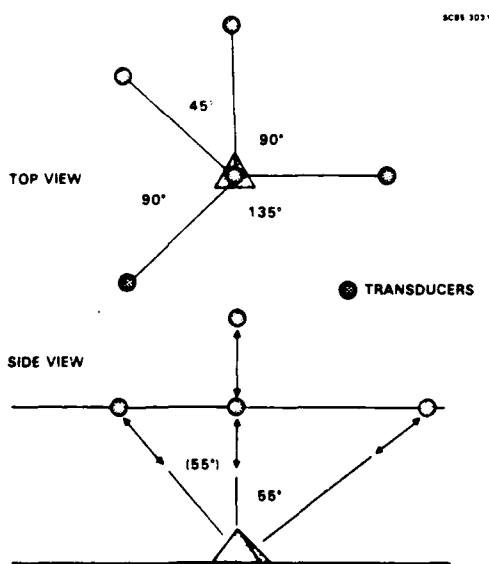


Fig. 16 Unsymmetrical transducer configuration.



Rockwell International
Science Center

SC5391.5FR

The method of solution, i.e., the determination of the most probable function, is based upon the iterative method discussed in the last section. The computational results are presented in Fig. 17. The three rows in these figures involved three different vertical scales relative to that of an ideal regular tetrahedron, namely 75%, 50%, and 25% of ideal. The first column in the figure presents the assumed tetrahedrons used in the preparation of the synthetic data. The second column presents the output of the imaging algorithm at the end

SC65 30543

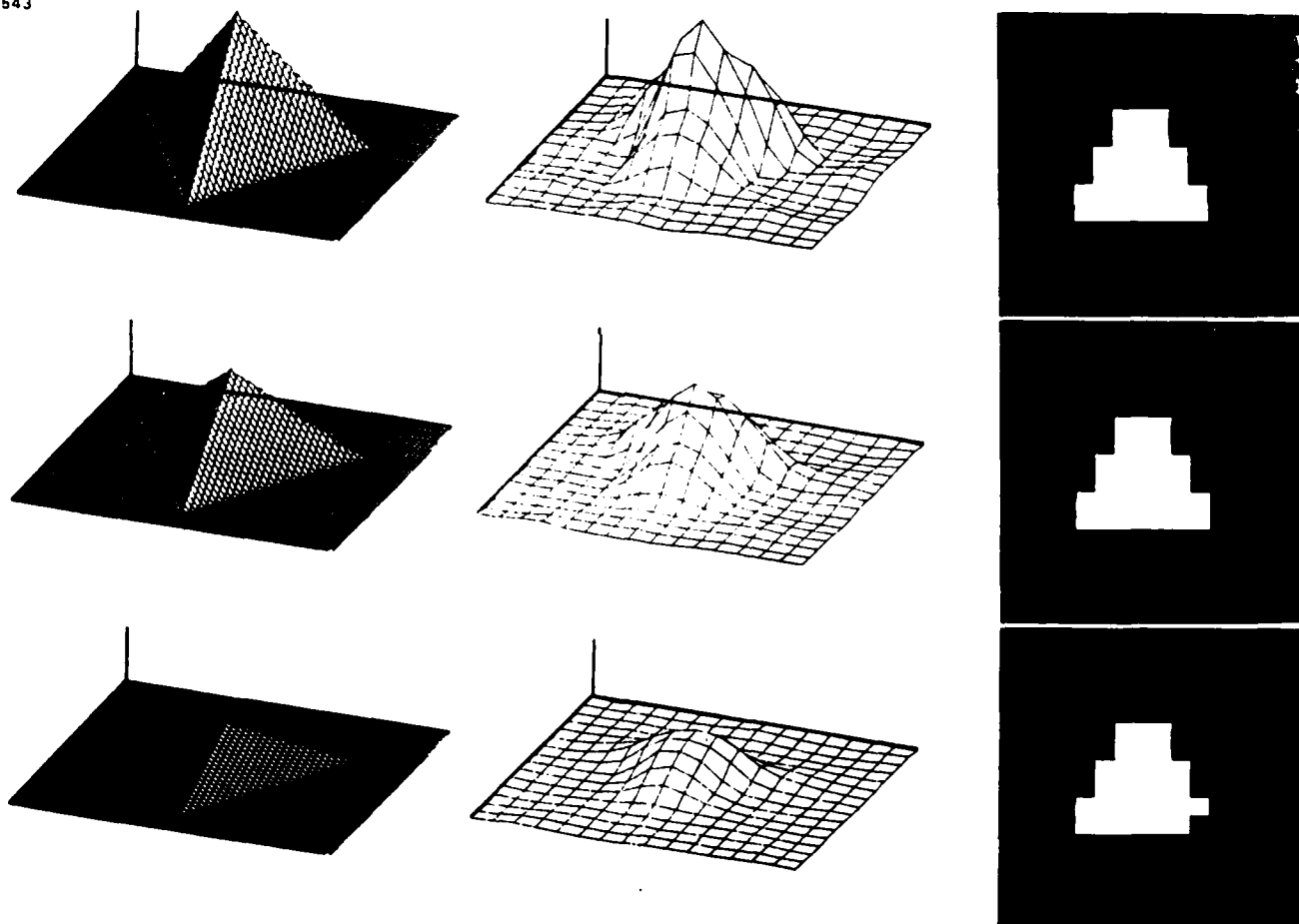


Fig. 17 Application of the iterative algorithm to squashed tetrahedrons of three different assumed heights.
(a) Assumed object, (b) Imaged object - hidden line representation, and (c) Imaged object - horizontal cross-section at 30% of maximum.



of the iterative procedure in the form of a hidden line presentation. The third column was a horizontal cross-section at 30% of maximum. The parameter sequence used in this procedure involved a mixture of the iteration procedures given in the last paragraph. Evidence of implicit interpolation is clear in k-space and somewhat less clear in super-resolution. The nonlinear nature of the measurement model with respect to the elevation function leads to an implicit generation of spatial Fourier transforms of the elevation function at spatial frequencies (i.e., points in k-space) different from those directly involved in the measurements.

We have attempted to simulate a hypothetical situation in which such a generation process does not occur by considering a measurement model linearized with respect to the entire elevation function - not just a correction to a previous estimate. The validity of this linearization is justified by taking an appropriately small value of the a priori variance of the elevation function. The output of an imaging algorithm based upon this modified measurement model is presented in Fig. 18, which shows clearly the poor performance obtained when the image contains only those spatial frequencies involved directly in the measurements.

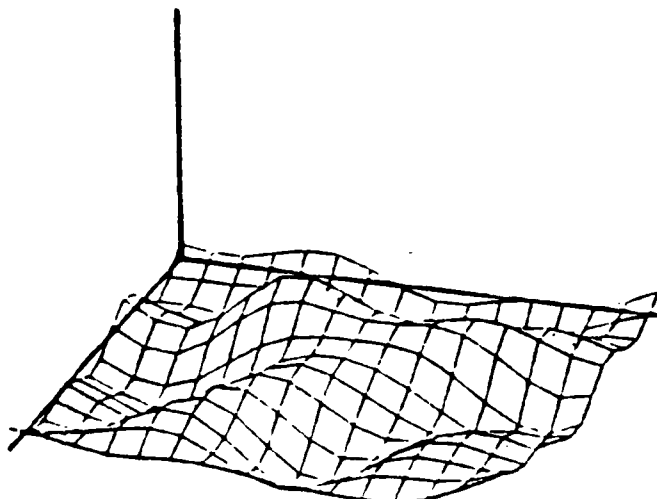


Fig. 18 Imaging with linearized measurement model.



We have considered a second computational example with the same unsymmetrical transducer configuration. This example involves test data based upon an assumed pair of hemispheres located near opposite corners of the localization domain as shown in Fig. 19. The imaging procedure involves the same iteration method that is used in the above discussion of the set of squashed tetrahedrons. The results are shown in Fig. 20. This imaging fidelity is quite satisfactory. This example illustrates the obvious fact that any number of objects can be present in the localization, and the resultant image is a clear indication that this can be done with high fidelity.

Fig. 19 Assumed hemispheres.

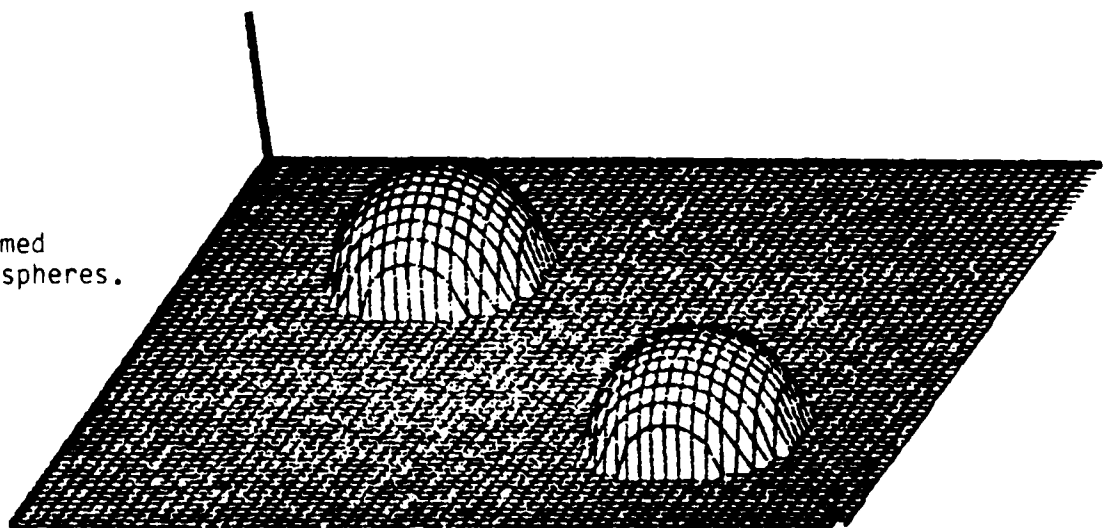
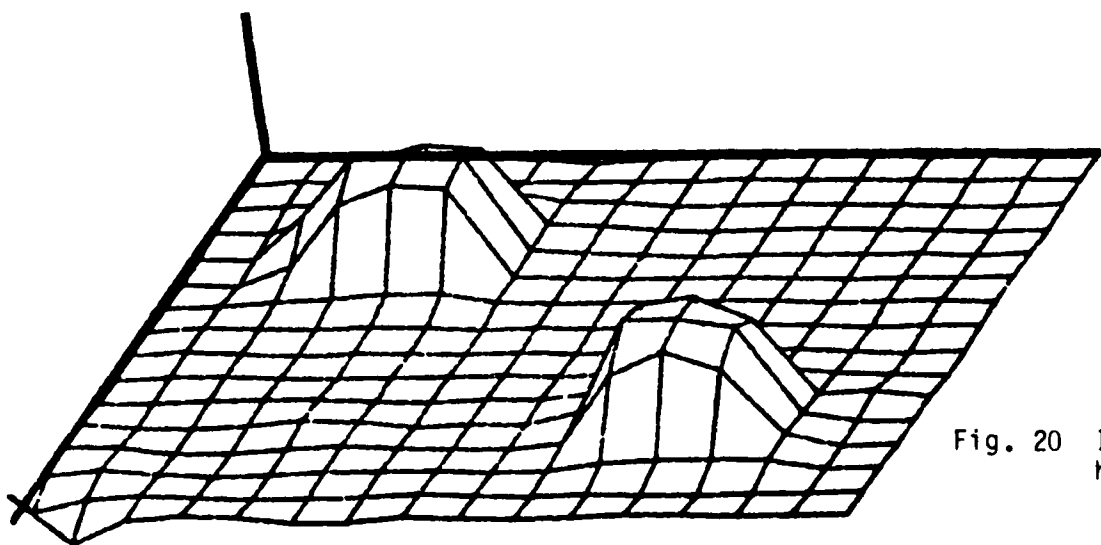


Fig. 20 Imaged hemispheres.





4.5 Ambiguity Theorems and Selection of Transducer Configurations

We turn now to a more detailed discussion of the ambiguity problems alluded to earlier. Here we are considering ambiguity only in a probabilistic sense, i.e., with a given set of input waveforms are two or more most probable images (of equal probability).

The probabilistic definition of ambiguity of concern to us in this discussion is given by the following detailed description. Let us consider a measurement system composed of a specified number of identical transducers, each operating in a pulse-echo mode, with specified positions and orientations. Let us also assume the localization volume to be in the far-field of each transducer and vice versa. To simplify our analysis let us restrict our attention to cases in which acoustical shadowing can be ignored for some reason (i.e., either it does not exist, its effects are negligible, or a double beam set-up is used). In this case, except for a multiplicative constant, the measurement model is mathematically identical to the model that would be obtained with the Born approximation. In this case the measurement model impulse response function (IRF) is proportional to the second derivative of the area function (AF). Let us further suppose that synthetic test waveforms are generated from assumed objects using the noiseless version of the above measurement model (even though we assume non-zero noise in the model used in the imaging algorithm). Finally, we assume that the a priori probability of the existence of an object is a function only of its volume (this is equivalent to the statement that the a priori statistics of a characteristic function $\Gamma(\vec{r})$ are given by the assumptions: (a) that the $\Gamma(\vec{r})$ and $\Gamma(\vec{r}')$ are statistically independent when $\vec{r} \neq \vec{r}'$ (\vec{r} and \vec{r}' are points on a specified 3D lattice spanning the localization domain), and (b) that $\Gamma(\vec{r}) = 0$ or 1 with probabilities independent of position.

Under the above assumptions, a probabilistic ambiguity can occur if there exist two or more assumed objects (objects involved in the generation of synthetic test waveforms) of equal volume that have identical sets of area functions (one for each incident direction).

Our first ambiguity theorem was discovered several years ago for the case of cylindrical objects of fixed length but random cross-section. Let us



SC5391.5FR

assume that the incident directions were chosen to be mutually orthogonal to each other and separately orthogonal to the cylinder axis, (i.e., the incident directions are \vec{e}_x and \vec{e}_y , and the direction of the cylinder axis is \vec{e}_z). In this situation, the stacked-plate ambiguity can occur. This is illustrated in Figs. 21a - 21c in which the order of a set of identical plates with nonidentical lateral positions is permuted. All of the objects have the same volumes and area functions. The generalization to other kinds of stacked plate ambiguities is obvious for the case where \vec{e}_x and \vec{e}_y are the incident directions. The plates do not have to be identical; ambiguities can occur if there is one subset of identical plates or, in fact, any number of different subsets of identical plates. These results can also be generalized to cases in which the incident directions in the xy-plane are nonorthogonal. From the inspection of Figs. 21a - 21c, the re-introduction of shadow zones can be seen to reduce the number of ambiguities but not necessarily to eliminate them altogether.

SC85-30043

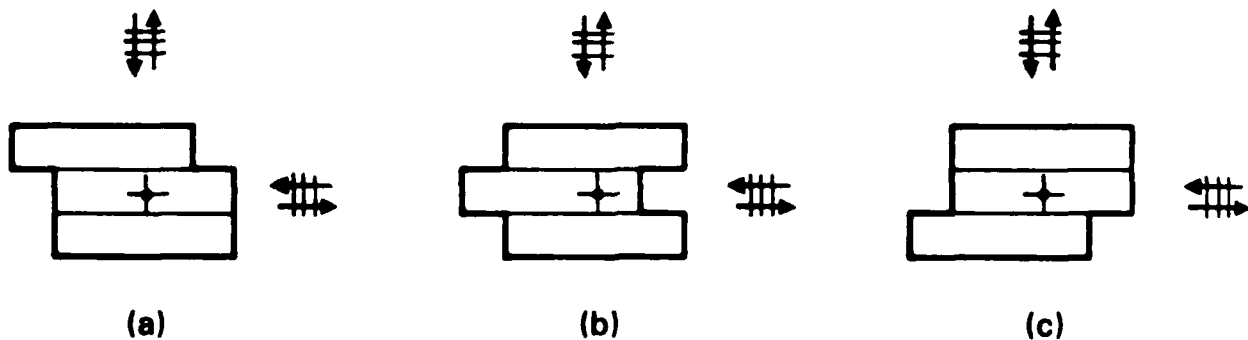


Fig. 21 Stacked plate ambiguity.

In any case, note the historical fact that the insufficiency of two incident directions in this 2D case led to the hypothesis that the minimum required number of incident directions is equal to the dimensionality plus one. This is presumed to be true for the Born approximation (valid either for a homogeneous inclusion with small property deviations or for a rigid body with



certain kinds of waveforms based upon pairs of oppositely directed beams). In spite of the ambiguities discussed later in this section, this hypothesis may still be true as long as the proper set of incident directions is selected to avoid ambiguities causing a significant degradation of imaging performance.

Another, apparently independent, type of ambiguity can occur when the measurement system possesses n-fold rotational symmetry about some axis. Let us consider again the simple case of cylindrical objects with various cross-sections observed by a measurement system with incident directions lying in the xy-plane. An example of a symmetric system is an arrangement of 3 transducers with incident directions in the xy plane with azimuthal angles 0° , 120° and 240° . In Figs. 22a and 22b we illustrate an ambiguity that can occur in such a system when separate measurements are made on two objects with equilateral-triangular cross section with their vertices displaced by a given angle counterclockwise and clockwise, respectively, from the incident directions. Each transducer in (a) will measure the same IRF and the same for (b). But what is most important is that the sets of IRF's in (a) and (b) are the same. This is easily seen from the fact that the triangle in (a) can be transformed to the one in (b) by reflecting it through an axis drawn through the origin in any of the three incident directions. Thus an imaging system based upon the present measurement system cannot distinguish between the two triangles.

SC85-30044

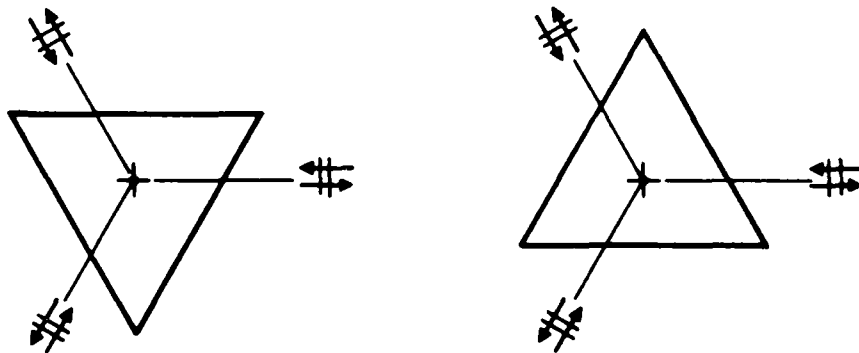


Fig. 22. Ambiguity associated with 3-fold rotational invariance.



SC5391.5FR

A number of generalizations can be derived in a fairly straightforward manner. Some of these are

- a. The ambiguities illustrated for the case of 3-fold symmetry are true for n-fold symmetry ($n > 2$).
- b. The same ambiguity theorem holds for n-fold symmetric system where the incident directions are not co-planar.
- c. The same ambiguity theorem holds when any number of transducers is eliminated.
- d. The theorem still holds when acoustical shadows are re-introduced.

Thus, clearly there is an important connection between ambiguity and symmetry of the measurement system. A reasonable supposition is that additional ambiguity theorems could be derived through a more comprehensive group-theoretical analysis of a wide variety of measurement systems.

In practice, we have found that when an ambiguity is present our imaging algorithms produce an average over the set of indistinguishable objects rather than picking one of them at random. An example of such behavior was encountered when we attemptd to image a tetrahedron using only four incident directions, corresponding to polar angles of 0° and 54.7° with azimuthal angles of 0° , 120° and 240° associated with the last polar angle. The reconstructed image was triangular when seen edge-on (as it should be), but the base was nearly circular instead of triangular. The resulting base shape evidently was due to a superposition of the two possible orientations of triangle which were consistent with the measurements. The fact that the base shape was nearly circular rather than two superposed triangles was probably due to the additional effect of smearing caused by the finite spatial resolution of the system.



SC5391.5FR

We have just discussed several ambiguity theorems in which waveforms arising from certain special sets of objects lead to ambiguities (i.e., the imaging algorithms cannot distinguish one member of a given set from another member). The question arises what effect does the existence of such ambiguities have on the imaging of an object not belonging to any of the special sets causing ambiguities with the measurement system being used? We do not have the answer to this question. However, the computer experiment discussed in the last section throws a little light on this question.

The motivation behind the choice of incident directions in Section 4.4.5 is now clear. The ambiguity associated with 4-fold rotational symmetry has been removed by selecting azimuthal angles with non-uniform spacing. However, the set of angles actually selected is a subset of a set of eight with 8-fold rotational symmetry. Thus, we are left with ambiguities associated with the latter symmetry. Since the "actual" object assumed in the generation of synthetic waveforms was a squashed tetrahedron which has 3-fold rotational symmetry about the z-axis, clearly the resultant waveforms do not produce a full-fledged ambiguity in either a 4-fold or 8-fold symmetric measurement system. We suppose that some kind of deterioration of the output image may be caused by this ambiguity. No mathematical proof of this supposition exists as yet, however, a distinct improvement of the computational results achieved by replacing the 4-fold symmetric measurements system by an unsymmetrical one suggests that this supposition is correct, as one can see in the comparison of the results of Section 4.4.5 with those of Section 4.4.4.



4.6 Calibration Procedure

4.6.1 Theoretical Considerations

In this section we present a theoretical analysis of calibration procedures. A more rigorous treatment of this material is contained in Appendix B in which a thorough analysis of scattering measurements and calibration procedures is presented. We will assume that the experimental setup as shown in Fig. 23 involves a single transducer operating in both transmit and receive modes or two transducers close together operating separately in transmit and receive modes. We will further assume that the transducer or pair of transducers is in the far-field of the localization domain and vice versa. Several further assumptions are made: namely that the host medium is a perfectly homogeneous, isotropic, lossless fluid (e.g., air) and that the localization domain is centered near the main axis of the incident beam.

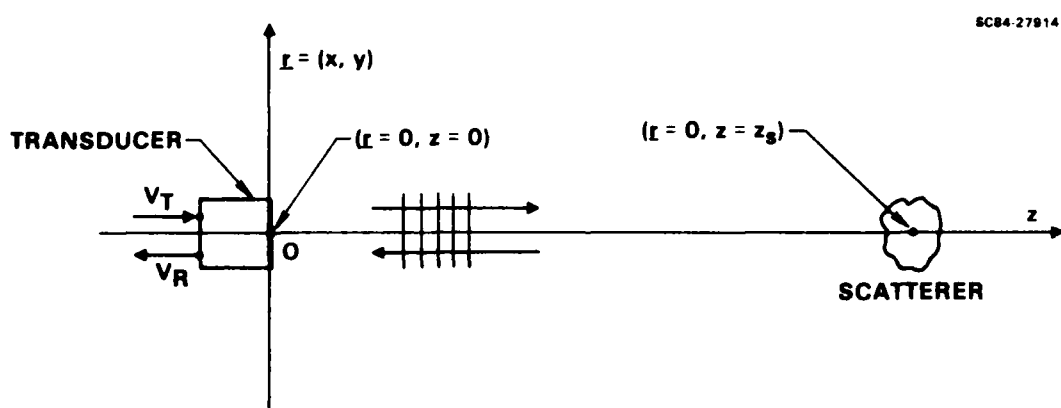


Fig. 23 Geometry of experimental setup.

Using the usual Fourier acoustics (FA) formalism (exactly analogous to Fourier optics) we express the pressure as a function of \underline{r}, z , and ω , i.e., $p = p(\underline{r}, z, \omega)$, where, as we have stated before, $\underline{r} = (x, y)$ is the transverse projec-



SC5391.5FR

tion of the 3-dimensional position vector \vec{r} and z is its longitudinal component, as shown in Fig. 7. As is usual in FA, the pressure can be represented either in the $(\underline{r}, z, \omega)$ -domain or in the $(\underline{k}, z, \omega)$ -domain where $\underline{k} = (k_x, k_y)$ is the transverse spatial frequency. The connection between these two representations is embodied in the relations

$$p(\underline{k}, z, \omega) = \int d\underline{r} \exp(-i\underline{k} \cdot \underline{r}) p(\underline{r}, z, \omega) \quad (1)$$

$$p(\underline{r}, z, \omega) = (2\pi)^{-2} \int d\underline{k} \exp(i\underline{k} \cdot \underline{r}) p(\underline{k}, z, \omega) \quad (2)$$

where $d\underline{r}$ and $d\underline{k}$ are differential area elements in \underline{r} -space and \underline{k} -space, respectively. The integrations in the above relations span all of \underline{r} -space and \underline{k} -space, respectively.

As discussed in Appendix B, the general wave $p(\underline{k}, z, \omega)$ can be split into right (+) and left (-) propagating waves in accordance with the expression

$$p(\underline{k}, z, \omega) = p_+(\underline{k}, z, \omega) + p_-(\underline{k}, z, \omega) \quad (3)$$

To save space during the remainder of this discussion, we will lean heavily on Appendix B. The transformations associated with the different functional parts of the system (transducer operating in the transmit mode, propagating from the transducer to the scatterer, the scattering process, propagating back to the transducer, transducer operating in the receive mode) are defined in Eqs. (15)-(24) in Appendix B. After combining these results we obtain the measurement system equation given by Eq. (25) in Appendix B repeated here for convenience:

$$\begin{aligned} V_R(\omega) &= \int d\underline{k} H^{\text{rec}}(\underline{k}, \omega) \exp(i\alpha_s) k^{-2} \int d\underline{k}' S_b(\underline{k}, \underline{k}', \omega) \\ &\times \exp(i\alpha' Z_s) H^{\text{tr}}(\underline{k}', \omega) V_T(\omega) \end{aligned} \quad (4)$$

In this equation the symbols (excluding those discussed earlier) are defined by



Rockwell International
Science Center

SC5391.5FR

$V_R(\omega)$ = voltage output of the transducer operating in the receiver mode,

$H^{rec}(\underline{k}, \omega)$ = transfer function representing the characteristics of the transducer operating in the receive mode,

$$\alpha = (k^2 - |\underline{k}|^2)^{1/2}, \quad k = \omega c^{-1}, \quad \omega > 0,$$

$S_b(\underline{k}, \underline{k}', \omega)$ = scattering matrix for backscatter of a right-propagating wave in the state (\underline{k}', ω) into a left-propagating wave in the state (\underline{k}', ω) ,

$$\alpha' = (k^2 - |\underline{k}'|^2)^{1/2},$$

$H^{tr}(\underline{k}', \omega)$ = transfer function representing the characteristics of the transducer operating in the transmit mode,

$V_T(\omega)$ = voltage input into the transducer operating in the transmit mode.

We stress that the above equation is exact, and as yet no far-field limitations have been imposed on it. We have omitted discussions of the evanescent forms of α and α' since this regime will be ignored in the later phases of our treatment.

We consider two cases: (1) a rigid reflector at $z = z_s$, and (2) a localized scatterer with its nominal center at $r = 0$ and $z = z_s$. In the first case we assume that the reflector is in the far field of the transducer (in both transmit and receive mode) but obviously not vice versa. In the second case we assume that the localized scatterer and the transducer are in the far-field of each other. In the rigid reflector case the back-scatter scattering matrix is given by

$$S_b(\underline{k}, \underline{k}', \omega) = k^2 \delta(\underline{k} - \underline{k}') \quad (5)$$



Rockwell International
Science Center

SC5391.5FR

The general result Eq. (4) above reduces to Eq. (4) in Appendix B namely

$$v_R^{\text{refl}}(\omega) = \frac{2\pi ik}{2z_s} \exp(2ikz_s) H^{\text{rec}}(0, \omega) H^{\text{tr}}(0, \omega) v_T(\omega) \quad (6)$$

In the second case, i.e., the case of the general localized scatterer, we obtain

$$\begin{aligned} v_R(\omega) &= -\frac{(2\pi)^2}{z_s^2} \exp(2ik(z_s + \delta z_s)) S_b(0, 0, \omega) \\ &\quad \cdot H^{\text{rec}}(0, \omega) H^{\text{tr}}(0, \omega) v_T(\omega) \\ &= -\frac{2\pi ik}{z_s^2} \exp(2ik(z_s + \delta z_s)) A_b(0, 0, \omega) \\ &\quad \cdot H^{\text{rec}}(0, \omega) H^{\text{tr}}(0, \omega) v_T(\omega) \end{aligned} \quad (7)$$

under the assumption that $|\delta z_s|/z_s \ll 1$. In the last line we have used the relation

$$S_b(0, 0, \omega) = \frac{ik}{2\pi} A_b(0, 0, \omega) \quad (8)$$

in which $A_b(0, 0, \omega)$ is the scattering amplitude for backscatter (i.e., pulse-echo).

Now let us consider two types of calibration procedures: (1) scattering from a single medium-to-large size rigid sphere is employed to determine the measurement system response function (MSRF) and (2) a combination of measurements involving a rigid flat plate and a small hard sphere is used to determine the MSRF. In the first type we assume that z_s is the distance to the center of the rigid sphere. Then we obtain

$$\begin{aligned} v_R^{\text{sph}}(\omega) &= -\frac{2\pi ik}{z_s^2} \exp(2ikz_s) A_b^{\text{sph}}(0, 0, \omega) \\ &\quad \cdot H^{\text{rec}}(0, \omega) H^{\text{tr}}(0, \omega) v_T(\omega) \end{aligned} \quad (9)$$



Rockwell International
Science Center

SC5391.5FR

We then obtain the MSRF to be given by

$$\begin{aligned} p(\omega) &\equiv -\frac{2\pi ik}{z_s^2} \exp(2ikz_s) H^{\text{rec}}(0, \omega) H^{\text{tr}}(0, \omega) V_T(\omega) \\ &= V_R^{\text{sph}}(\omega) / A_b^{\text{sph}}(0, 0, \omega) \end{aligned} \quad (10)$$

where $A_b^{\text{sph}}(0, 0, \omega)$ is the scattering amplitude for the rigid sphere. The latter quantity must be obtained theoretically because the experimental measurement of it will involve the same MSRF we are ultimately trying to determine. So far, the theoretical results for the scattering amplitude of the rigid sphere are available only in the Rayleigh regime, i.e., in the frequency interval where the wavelength is large compared with the sphere diameter. Unfortunately, this regime entails problems associated with low signal-to-noise ratios.

Until the theoretical analysis of scattering of acoustic waves from a rigid sphere is complete, we have opted for a hybrid procedure in which the MSRF for a fixed range is determined by measuring the reflection from a rigid flat plate. The motivation behind the hybrid procedure is that the reflection from the rigid flat plate has a very high signal-to-noise ratio and thus could provide a rich set of inferences concerning the nature of $p(\omega)$ (aside from an unknown time shift, which we will later define as zero) for a single transducer. We will either assume that the transducers in various positions are identical or assume that a single transducer is used in all positions. The corrections of the distance between each transducer (or a single transducer in each position) and the origin will be determined by a relatively low signal-to-noise measurement of the scattering from a small rigid sphere to determine the distance correction. In the latter case only one quantity is to be estimated and therefore should obtain an adequate estimate in the face of low signal-to-noise ratios.



SC5391.5FR

Preliminary tests indicate that the first of these deficiencies can be overcome by using a different excitation pulse for the transmitters. The remaining deficiencies will need further research effort. In principle, they could be overcome by the use of sufficiently strong pulses spaced sufficiently far apart. In practice, however, limitations in the size of pulses are due to such considerations as saturation of amplifiers and damage to transducers. One could simulate the effect of a large pulse using the pulse-compression techniques in which the transmitted pulse is spread out in time and is reconstituted after reception. An extreme example of this would be to send a series of pure tones at a sufficient number of different frequencies to satisfy the Nyquist criterion for reconstructing the desired pulse in the time domain. These and other possibilities will be investigated in the second phase of the program.

2. To find a way of relaxing the bandwidth requirements of the measurement system for imaging objects with a given range of spatial scale. The bandwidth requirements of the current algorithms are rather severe: they dictate that the transducer should respond to wavelengths from about six times the largest dimension of the object down to wavelengths comparable to the finest structure of the object. One possibility is to use a much larger diversity of incident directions, since numerical experiments have shown that under these conditions one may relax the lowest frequency requirement. This would necessitate a somewhat different approach in the inversion in order to bring the computation time within reasonable bounds. Another possibility is to make use of pitch-catch measurements (i.e., sending and receiving on two different transducers), since this provides information on lower spatial frequencies than is possible for pulse-echo.



Rockwell International
Science Center

SC5391.5FR

A substantial effort has been expended on the experimental problems of obtaining reproducible waveforms conforming to the related requirements of high reproducibility and low noise (both systematic and random). This is discussed at considerable length in Section 4.7 where a number of approaches to these problems are considered. These matters impinge on the problem of choosing transducer configurations, since minimizing the pulse-echo returns from the bare reflective table is important.

Item (a), i.e., the attainment of large bandwidth, is an important problem because the use of a sparse set of transducers means each waveform must represent a wide spectrum of wavelengths, matched in an appropriate way to the spectrum of characteristic lengths of the possible objects. This requirement must be met without a significant loss of the efficiency of coupling between the transducer and air. Loudspeaker technology appears to provide the answer since stereo systems are subject to the same general requirements.

The ultimate success of our acoustical imaging approach in an operational context requires the raising of both experimental technique and signal conditioning to a new level of refinement.

5.4 Problems to be Addressed

In the following paragraphs we present a list of important problems whose solutions are in various stages of development but are not yet complete.

1. To improve the quality of experimental waveforms. Deficiencies in experimental waveforms used in inversions to date are:
 - a. restricted bandwidth (50%)
 - b. background noise
 - c. ringing in the transducers
 - d. reverberations from previous pulse(s).



SC5391.5FR

torily without any apparent tendency to "jump the track." The sequence of images (i.e., estimated elevation functions) produced in the iteration process showed a steadily increasing sharpness and resolution. The final image showed definite indications of super-resolution and implicit k-space interpolation (i.e., the inferring of Fourier components of the image at spatial frequencies different from those involved directly in the measurement). In the last set of computational examples (Section 4.4.5) we assumed an unsymmetrical transducer configuration avoids certain probabilistic ambiguities associated with rotational symmetry. The results showed a significant improvement in resolution and in one case a striking removal of spurious artifacts.

All of the algorithms, except for the second one, have been tested with synthetically generated waveforms, instead of experimental waveforms. Such synthetic test data used the Kirchhoff approximation in its generation and thus, since the same approximate scattering theory is used in both the test data and the imaging algorithm, the effect of Kirchhoff errors is not assessed. However, in the case considered in connection with the third and fourth algorithms, we believe that the consequences of Kirchhoff error are negligible.

5.3 Experimental Techniques and Calibration

The production of experimental waveforms of adequate quality involves several significant problems, namely the achievement of (a) correct amplitudes as referred to an absolute scale, (b) adequately low noise (both systematic undesired signals and random noise), and (c) large bandwidth. Problem (a) is widely believed in the acoustical community to be insuperably difficult; however, we have been obtaining signals with amplitude accuracy (not just relative accuracy) for many years. One of the main keys to success here is a good calibration procedure based upon an accurate mathematical model of all of the processes involved. Such matters are discussed at length in Section 4.6 and in Appendix B. The second key to success is a highly reproducible measurement procedure, the attainment of which entails close attention to problem (b) dealing with systematic and random noise.



SC5391.5FR

The second stage involved the application of the CLEAN algorithm (used originally in astronomical imaging) to get rid of undesirable side lobes. The last stage of this algorithm involved the use of a thresholding operation applied to the "CLEANed" image. The ad hoc nature of this algorithm is related in part to the fact that the object should be represented by a form characteristic function that does not enter the picture until the thresholding operation at the end. Because of this deficiency the algorithm is incapable of super-resolution.

The third and fourth algorithms are based upon a simpler and somewhat restricted representation of solid objects, namely in terms of single-valued elevation functions with the additional assumption that the objects are effectively flat-bottomed. The third algorithm (see Section 4.3.4) used a modified version of the conjugate vector method to obtain the most probable elevation function given the measurements. The behavior of this algorithm was not entirely satisfactory, possibly due to the failure to meet sufficiently well the requirements for the validity of the conjugate vector method and possibly certain other effects. In any case, this algorithm was set aside for further investigation at a later time.

The fourth algorithm (see Section 4.4) employs an entirely different approach to the implementation of the same basic concept. This approach involves an iterative technique in which both the experimental waveform and measurement system response are initially subjected to the smoothing operation and in which later stages of the iterative process involve successive unsmoothing combined with linearization of the measurement model with respect to the corrections of the elevation function. To simplify the analytical and computational work we assumed that the elevation function was a Gaussian random process a priori, although the incorporation of a positivity bias would have been appropriate. In practice we considered more general iteration strategies than we have implied in the above remarks; namely, we have considered the variation of the a priori standard deviation of the elevation function and measurement noise. In many cases it was expedient to use the output of the second algorithm as an initial estimate. In the computational examples this method converged satisfac-



SC5391.5FR

image at spatial frequencies different from those directly involved in the measurements. A more detailed discussion of item (a), i.e., the development of implementation approaches, is included in the next section on imaging algorithms.

5.2 Discussion of the Four Imaging Algorithms

In the following paragraphs we discuss the four imaging algorithms involved in the present DARPA program. Although the fourth algorithm was the most successful, the previous three have not been abandoned. We have included all four algorithms in Section 4.0 on progress. Each algorithm has its own peculiar merits, and conceivably future progress may entail combinations of the methodologies represented by these algorithms individually or perhaps even the further development of any single one.

In the beginning of the present DARPA supported program the inclusion algorithm discussed in the last section was adapted to the case of acoustical imaging of solid objects in air using the Kirchhoff approximation. By using pairs of oppositely directed beams yielding waveforms combined in a particular ways (see Section 4.3.2) a simplified measurement model that is mathematically identical (except for a factor of two) to a model based upon the Born approximation could be obtained. This algorithm used the characteristic function representation of the object. This algorithm involved the essential use of the conjugate vector method. This choice of representation in 3-dimensional space led to an information content (i.e., number of bits) in the state of the object that was sufficiently burdensome to make the conjugate vector method excessively time consuming.

A similar, but not identical, representation was used in a second imaging algorithm (see Section 4.3.3) that is somewhat ad hoc from a decision-theoretic point of view but that is much faster computationally. This algorithm used in the first stage a conventional imaging algorithm to estimate a pseudo-characteristic function (the word "pseudo" is used to signify the fact that this function was not limited to the values 0 and 1 at each point in space but would be expected to approach a true characteristic function certain ideal limits).



SC5391.5FR

reduction of the amount of experimental data while maintaining a given imaging quality is a widely held view among investigators using probabilistic approaches in the field of imaging and inversion. Our first breakthrough, several years ago, was to obtain a feasible algorithm for imaging a weakly scattering inclusion in a solid where the included material was known a priori but not the boundary geometry. The attainment of a feasible algorithm was made possible by the application of the so-called conjugate vector method, which because of space limitations cannot be discussed here (see Section 4.3.2). At this time the "stacked plate" ambiguity was discovered, an advance in understanding that led to the hypothesis that four is the minimal number of incident directions for pulse-echo scattering measurements needed for the imaging of a 3-dimensional weakly scattering inclusion at least in the limit of large signal-to-noise ratio and large bandwidth. However, what set of incident directions should be chosen was not very clear, outside of the fact that oppositely directed pairs are redundant in the Born approximation.

Prior to the start of the DARPA program, the inclusion measurement model was subjected to minor modifications in mathematical structure to become the general measurement model to be used for the case of solid objects in air. However, the underlying physical assumptions underwent major modifications in proceeding from the case of weakly scattering inclusions (for which the Born approximation is valid) to the case of strongly scattering solid objects in air (for which the Kirchhoff approximation is presumed to be appropriate). A derivation of the latter measurement model from first principles is presented in Appendix A.

During the period of the present DARPA program, the contributions to the "distributed" breakthrough consisted of two main items: (a) the development of a combination of analytical and computational methods yielding a potentially practical implementation of the general probabilistic concept and (b) the discovery of new types of probabilistic ambiguities, an advance in understanding leading to more effective choices of transducer configurations and to a deeper insight concerning the nature of the inference of Fourier components of the



5.0 DISCUSSION AND TECHNICAL SUMMARY

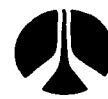
In this section we will put our accomplishments in perspective; i.e., what did we know at the beginning of the program, what do we know now, how does our present state of advancement in methodology compare with those of competing programs elsewhere, and finally what questions remain to be answered?

5.1 Nature of the Breakthrough

From an outside point of view our accomplishments can be regarded as a breakthrough in the technique of imaging of solid objects in air. However, from an inside point of view the whole process seems far less dramatic and is perceived to consist of a rather slow evolution punctuated with little spurts of understanding, corrections of previous errors, recognition of previously unrecognized limitations, etc.

To return to the outside point of view, the breakthrough consists of the acoustical imaging (i.e., determination of the external geometry) of solid objects in air with a set of transducers that is very sparse relative to the set that would be required for an imaging algorithm based upon conventional ideas. This sparseness is made possible by the full use of the complete waveform and the a priori information embracing the obvious fact that each volume element (voxel) in 3D space is occupied either by solid material or by air with specified a priori probabilities. As far as we know, this accomplishment is unique - except for our own previous efforts. In making this statement we have defined the word "image" to imply the use of an ensemble of nonparametric models (i.e., such an ensemble contains every conceivable model represented on a specified grid within a specified localization domain. A significant amount of attention has been devoted by other investigators (e.g., Tsai et al., 1984) to the case in which the ensemble of possible objects is composed of parametric models involving a limited number of adjustable parameters. Because of its parametric nature we do not regard this type of approach as a true imaging procedure.

From an inside viewpoint this breakthrough has been spread out over many years of effort. The general ideal that a priori information can allow a



Rockwell International
Science Center

SC5391.5FR

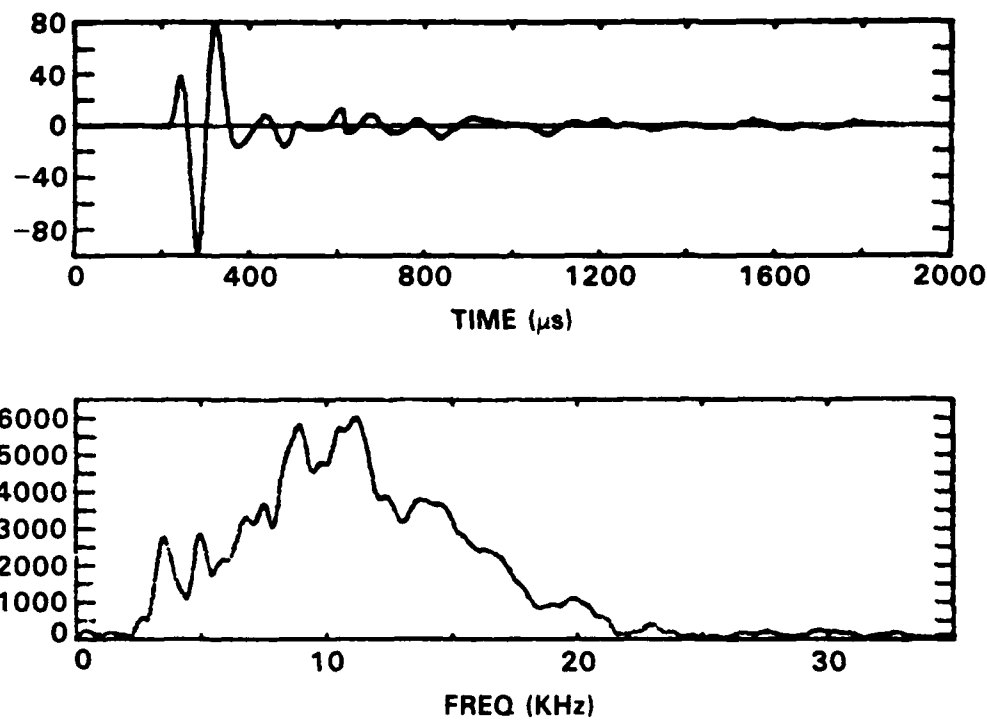


Fig. 27 Response of tweeter to square pulse.

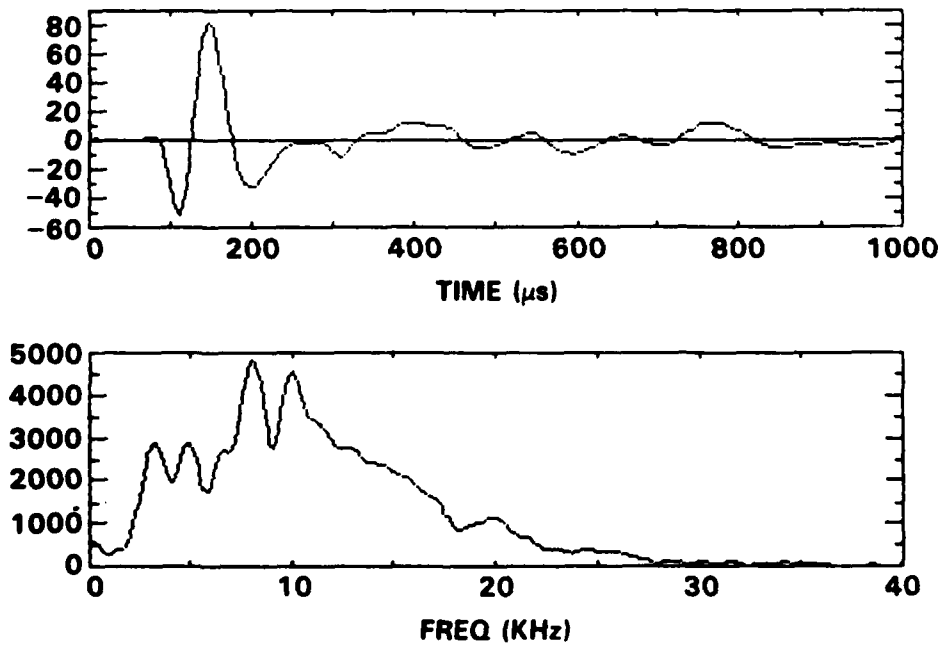


Fig. 28 Response of tweeter to step function.



4.7.4 Unipolar Transducer Excitation

The relatively large bandwidth obtained for so small a device described above is quite notable. However, the requirements for extreme bandwidth and power strains the performance limits of this approach.

Yu, et al., have described an experimental technique of excitation in which ultrasonic unipolar pulses are produced by planar ceramic piezoelectric transducers by applying a step voltage to the transducer electrodes, rather than a unipolar electrical pulse. Approaching the theoretically predicted results requires appropriate impedance relationships, both electrically between the transducer and source or receiving electronics, and acoustically between the transducer and the medium into which sound is transferred. This approach appeared to be rather easily implementable for air acoustics, and results are presented below.

Excitation of a commercial high frequency speaker (tweeter) directly from a 50 ohm square wave pulse generator is shown in Fig. 27a, with the frequency response shown in Fig. 27b. The observed bandwidth is less than 50% corresponding to less than a 2:1 ratio between the highest and lowest usable frequencies. The pulse width is chosen to maximize the transducer response. The receiver transducer used the FET preamplified PVF₂ unit described above. Exciting the same transducer with a step voltage directly from a 50 ohm source generator resulted in the waveform and frequency response in Fig. 28. The useful bandwidth now corresponds to a ratio of highest to lowest frequencies which exceeds 10:1. This result, together with the high peak power handling capability, is a promising development in hardware for active acoustic imaging.

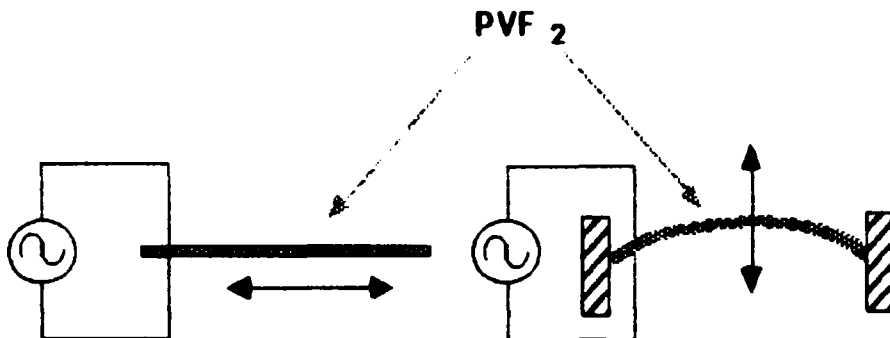


Fig. 25 Excitation of compressional waves using d13 mode in polymer film transducers.

The static capacitive reactance of the film is ~ 150 Kohms, which results in a poor electrical match to a pulsing source, but which is compatible with high impedance FET preamplifier receiver electronics. To obtain a robust output pulse, a miniature audio transformer is used to improve the match between the transducer and the 50 ohm pulsing unit. As just stated, a FET preamplifier solves the receiver problem handily, and provides a 50 ohm impedance level output for further signal conditioning and processing.

A typical pulse response for transmission between two such transducers is shown in Fig. 26a. The spectral response of this pair is shown in Fig. 26b.

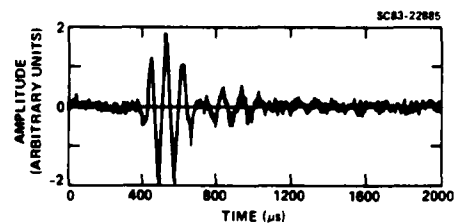
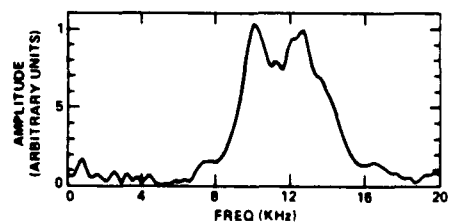


Fig. 26

- (a) Typical echo waveform obtained with transducer pair,
- (b) frequency response of transducer pair.





Rockwell International

Science Center

SC5391.5FR

Note that such acoustic isolation would not be possible if a single transducer were used in conjunction with a T/R switching circuit. The ring-down signal would mask the echo.

4.7.3 Additional Transducer Technology

The optimal transducer requirements for the imaging techniques investigated in this program include maximum bandwidth and high signal-to-noise ratio. The former provides for a wide range of k-vectors along each incident direction to give the most detailed information about the object features. The latter is necessary for good image fidelity. In addition, the higher the signal-to-noise ratio the larger the effective bandwidth (unless the transducer bandpass has vertical sides), since a large portion of the bandpass will be above the noise.

The transducers were fabricated from PVF₂ (polyvinylidene difluoride), a piezoelectric polymer with low acoustic impedance and moderately high loss tangent. These properties lend themselves to pulse applications in air, where the acoustic impedance is quite low and large bandwidth is required. In particular, when large bandwidth is required in the audio range, structural packaging becomes critical, and multi-element speaker/transducer elements and cross-over networks between them are required, viz., the high fidelity speaker. Such size and weight constraints imposed by this technology are unacceptable for most of the intended application areas for acoustic imaging, such as robotic manufacturing and image processing.

The transducer element, by itself (Fig. 25), is a 54 μ thick film, metalized on both sides, measuring 1.5 cm \times 0.75 cm. The stretch direction, i.e., the axis of piezoelectric transverse dilatation, is the long dimension. The film is formed into a shallow arch, approximately 3 mm in height. Since the film is clamped at both ends, the dilatation is mechanically transformed into a pulsing motion in the arch direction. This mechanical transformation permits the excitation of compressional sound waves.



SC5391.5FR

Additional measures were taken to suppress the effects of randomly generated noise by signal averaging. The standard prescription used was to average 256 successive waveforms.

4.7.2 Suppression of Systematic Noise

The experimental data were taken in a normal laboratory environment in which no precautions were taken to reduce ambient noise or to suppress reflections from walls, floor, etc. For a given structural arrangement - which necessarily includes the transducers, the object (always suspended from the ceiling), and the robot, which was used to position the transducers, systematic signals could be observed that were found to be echoes from various surfaces (sometimes undetermined). When the culprit surfaces were determined, absorbing mats were suitably placed.

Another type of systematic intrusive signal was determined to come from some unlocatable surface in which the echo observed was generated by a prior pulse. This was proved by varying the pulse rate to determine that the offending signal could be time shifted by the amount of change in the pulse rate time delay.

This problem was treated by reducing the pulse repetition rate enough to ensure that the room "reverberation" had sufficiently dissipated. Rates as low as 0.5 pulses per second were used. Alternatively, by means of software control, triggering can be executed with a randomizing function, and by means of signal averaging, such systematic echoes can be effectively randomized.

A layer of acoustic foam material provided a measure of acoustic isolation between the transmitter and receiver, in order to reduce the residual ring-down, which can be comparable to or larger than the echo scattered from the object, despite the relatively long time delay. Because the transducer elements are effectively one half-wavelength in dimension, the resulting field pattern is fairly omnidirectional, so that lateral transmission between the adjacent transducers is still significant unless precautions for acoustic isolation are taken.



SC5391.5FR

4.7 Progress in the Production of Experimental Waveforms

The problems encountered in the production of experimental waveforms can be grouped into two main categories, namely noise suppression and the problem of obtaining a suitably large bandwidth. The noise originates from several causes, and includes random noise from background sources (e.g., equipment, air conditioner, etc.), reverberations around the room due to the previous pulse, the ringdown of the signal transmitted between adjacent transducers. We now discuss each of these effects in more detail.

4.7.1 Suppression of Random Noise

Random noise from background sources was treated by baffling the transmit/receive pair of transducers with an acoustically absorbing material (Indasco E-1-25-PSA). The material is supplied in foam sheets, which lends itself to building up successive layers in desired shapes. Figure 3 illustrates the approach used.

As shown in Fig. 24, a "hood" was placed over the transducer set to restrict the effective field of view. Similarly, absorbing material was placed around and behind the transducer elements to suppress signal reflections generated from the packaging and mounting structure. Qualitative investigation of this sensitivity to mounting indicates that a great deal of care is required and improvement is possible in avoiding resonant effects due to the mechanical nature of the device packaging.

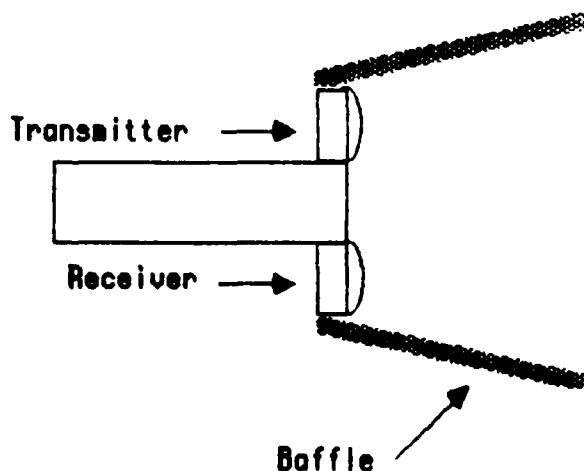


Fig. 24 Transducer module with acoustic baffle.



SC5391.5FR

From (6) we obtain the MSRF in the simple form

$$p(\omega) = -\frac{2}{z_s} v_R^{\text{refl}} \quad (11)$$

in which the distance from the transducer to the plate is assumed to be z_s .

In the actual measurement system involving an unknown object we must assume that the distances from the various transducers to the origin of the laboratory coordinate system will deviate from z_s , say $z_s + \delta z_s$ in the case of particular transducer, whereupon $p(\omega)$ must be replaced by $p(\omega) \exp(2i\omega c^{-1} \delta z_s)$. The calibration measurement involving a small rigid sphere (assumed, by definition, to be centered at the origin) led us to consider the measurement model

$$f(\omega) = p(\omega) \exp(2i\omega c^{-1} \delta z_s) \alpha a^3 \omega^2 + v(\omega) \quad (12)$$

where $\alpha a^3 \omega^2$ is the scattering amplitude of a rigid sphere of radius a in the Rayleigh regime and where α is a constant dependent upon the acoustical properties of air.

The best estimate of δz_s for a particular transducer can be obtained by a standard maximum likelihood procedure based upon the above measurement model. In the case where δz_s is sufficiently small that the exponential function can be linearized with respect to its argument $2i\omega c^{-1} \delta z_s$, one can obtain a best linear estimate of δz_s by straightforward analytical means. If αa^3 is not known with adequate precision then one can derive best linear estimates of both αa^3 and $2\alpha a^3 \omega c^{-1} \delta z_s$.

4.6.2 Implementation

The above procedure has now been implemented in software on the VAX 11/780, and tested with synthetic and experimental data. The inputs to the algorithm consist of the measured waveforms for the calibration sphere and flat plate, together with the radius of the sphere and distance to the plate. The output consists of the fully calibrated reference waveform, referred to a spatial origin corresponding to the center of the calibration sphere.



SC5391.5FR

3. To arrive at a fundamental understanding of potential ambiguities associated with a given measurement system. Or: Given a certain localization volume which we wish to image at a certain resolution, how many incident directions do we need, and how should they be arranged? Our original contention, that in the Born approximation any set of four noncollinear directions would suffice in 3 dimensions, we now know to be incorrect. If indeed four incident directions are sufficient, they have to be chosen with considerable care in order to avoid high-order symmetries which would render the imaging system incapable of distinguishing between some orientations of objects with corresponding symmetry.
4. To derive theorems complementary to the ambiguity theorems. Using more and more ambiguity theorems as a guide to choosing incident directions is unreliable because of the uncertainty of deriving or discovering all of them. Pursuing a more direct approach to the understanding of the implicit process of deducing spatial Fourier transforms of the elevation function at other spatial frequencies is desirable, however,
5. To arrive at a procedure for selecting automatically the sequence of successive unsmoothing filters used in the iterative imaging method.
6. To determine the effect on image fidelity of errors resulting from the use of the Kirchhoff approximation.
7. To devise a computationally tractable method of dealing with objects with acoustical shadows.
8. To investigate the feasibility of improved scattering models. An approach currently being considered in the course of our Independ-



Rockwell International
Science Center

SC5391.5FR

dent Research and Development Program involves the use of the Pontryagin maximum principle, which we believe is capable of producing a computationally tractable exact solution to the inversion problem for a rigid scatterer in air. A successful implementation of this approach would render obsolete items 6. and 7. above.

9. To improve the elevation function correction procedure. For objects described by single-values elevation functions, the present formulation terms of $z = Z(\underline{r})$, where $\underline{r} = (x,y)$ gets into difficulties if the slopes are too steep. A need exists for a revised representation in the context of the iterative procedure where the correction in the elevation function at a given position \underline{r} is made in the local normal direction rather than in the vertical direction, as is presently done.
10. To improve algorithmic efficiency. Our investigations of acoustical imaging so far have emphasized a "proof of principle" point of view. Accordingly, we have not placed a heavy emphasis on computational efficiency. In the future this aspect of the project must be given a much higher priority.



**Rockwell International
Science Center**

SC5391.5FR

6.0 APPENDICES

In the following two appendices we discuss the mathematical foundations of the general measurement model (APPENDIX A) and the analysis of the measurement system response function based on Fourier acoustics (APPENDIX B).



Rockwell International
Science Center

SC5391.5FR

APPENDIX A

KIRCHHOFF APPROXIMATION AND AREA FUNCTIONS

The purpose of this section is to present a discussion of the theory of the Kirchhoff approximation applied to the backscattering of acoustical waves in air from a rigid object and to derive an alternative form of this result expressed in terms of the area function. We will first derive the scattering amplitude and impulse response function for an isolated body. Later, we will derive these quantities for the case of a rigid object resting on a rigid (i.e., highly reflective) table.

We assume that the rigid object occupies the domain, \mathcal{D}^S whose surface is \mathcal{S}^S . The pressure $p = p(\vec{r}, \omega)$ at any point \vec{r} in the air outside of the domain \mathcal{D}^S and at the frequency ω , satisfies the well-known Helmholtz equation

$$(\nabla^2 + k^2) p = 0 \quad (1)$$

where $k = \omega/c$ in which c is the propagation velocity of sound in air. The implicit time factor is assumed to be $\exp(-i\omega t)$. We will define the incident pressure p^i as the field that would be produced by the transducer in the absence of the object and define the scattered pressure p^S as the correction to the incident pressure p^i due to the presence of the object. Both p^i and p^S must separately satisfy Eq. (1) for all $\vec{r} \neq \mathcal{D}^S$.

The scattered wave, p^S , must satisfy the usual radiation condition at large distances, i.e.,

$$\nabla p^S \rightarrow i \vec{e}_r k p^S \quad (2)$$

as $r \rightarrow \infty$. The unit vector \vec{e}_r is defined by

$$\vec{e}_r = \vec{r}/r \quad (3)$$



SC5391.5FR

where $r = |\vec{r}|$. On the surface \mathcal{S} the total pressure must satisfy the boundary condition

$$\vec{n} \cdot \nabla p = 0, \quad (4)$$

where \vec{n} is the outwardly pointing normal vector to the surface. The above condition implies that the normal component of velocity vanishes everywhere on the surface of the object.

It will be necessary in the later development to consider the Helmholtz Green function $G = G(\vec{r} - \vec{r}', \omega)$ defined by the relation

$$(\nabla^2 + k^2) G(\vec{r} - \vec{r}', \omega) = \delta(\vec{r} - \vec{r}') \quad (5)$$

with the above radiation condition at large distances. It is well known that

$$G(\vec{r}, \omega) = -\frac{1}{4\pi r} \exp(ikr) \quad . \quad (6)$$

A straightforward application of Green's theorem and the use of Eq. (1) with p^s substituted for p yields the result (see Baker and Copson, 1950)

$$p^2(\vec{r}, \omega) = \int d\vec{S}' \cdot [G(\vec{r} - \vec{r}', \omega) \nabla' p^s(\vec{r}', \omega) - p^s(\vec{r}', \omega) \nabla' G(\vec{r} - \vec{r}', \omega)] \quad . \quad (7)$$

Relating p^s to p^i by means of the boundary condition (4), we obtain the desired result

$$p^2(\vec{r}, \omega) = - \int d\vec{S}' \cdot [G(\vec{r} - \vec{r}', \omega) \nabla' p^i(\vec{r}', \omega) + p^s(\vec{r}, \omega) \nabla' G(\vec{r} - \vec{r}', \omega)] \quad . \quad (8)$$

With $\vec{r} \in \mathcal{S}$, the above expression is a boundary integral equation to be solved for p^s on \mathcal{S} . The pressure in the scattered wave at any point outside of \mathcal{S} is given by the same equation with $\vec{r} \notin \mathcal{S}$.



SC5391.5FR

The Kirchhoff approximation involves two assumptions: (a) $p^s = p^i$ on \mathcal{S}^i , the part of the surface \mathcal{S}^s illuminated by the incident wave (in the geometrical optics limit) and (b) the integrand of the integral in (8) is negligible on the remainder of the surface \mathcal{S}^s . The introduction of these assumptions into the left hand side of (8) yields the expression

$$p^s(\vec{r}, \omega) = - \int_{\mathcal{S}^i} d\vec{s}' \cdot [G(\vec{r} - \vec{r}', \omega) \nabla' p^i(\vec{r}', \omega) + p^i(\vec{r}', \omega) \nabla' G(\vec{r} - \vec{r}', \omega)] \quad (9)$$

in which the r.h. side is no longer dependent on p^s and hence known if \mathcal{S}^i is given (p^i is always assumed to be given).

We now assume that the incident pressure is a plane wave propagating in the direction \hat{e} , namely

$$p^i(\vec{r}, \omega) = \exp(i\vec{k} \cdot \vec{r}) \quad (10)$$

where $\vec{k} = k\hat{e}$. We also confine our attention to the pulse-echo case in which the observation point is assumed to be given by

$$\vec{r} = -r\hat{e} \quad . \quad (11)$$

It is appropriate to require that the origin of the coordinate system be placed in or near \mathcal{D}^s .

If r is sufficiently large (more specifically, if the observer is in the far field of the scatterer), we can write

$$G(\vec{r} - \vec{r}', \omega) \approx -\frac{1}{4\pi r} \exp(ikr) \exp(ik\hat{e} \cdot \vec{r}') \quad . \quad (12)$$

Substitution of this approximation into (9) yields the result

$$p^s(-r\hat{e}, \omega) = \frac{1}{2\pi r} \exp(ikr) \hat{e} \cdot \int_{\mathcal{S}^i} d\vec{s}' \exp(2ik\hat{e} \cdot \vec{r}') \quad . \quad (13)$$

Using the definition of the scattering amplitude $A(\omega, \hat{e})$ for backscatter, namely



SC5391.5FR

$$p^2(-r\vec{e}, \omega) = \frac{1}{r} \exp(ikr) A(\omega, \vec{e}) ,$$

we deduce that

$$A(\omega, \vec{e}) = \frac{ik}{2\pi} \vec{e} \cdot \int_{\mathcal{S}^i} d\vec{S} \exp(2ik\vec{e} \cdot \vec{r}) , \quad (14)$$

a well known result.

We will now transform the last result into a more convenient form. The first step is to continue the surface integration over a closed surface containing both the body and the acoustical shadow. This procedure is illustrated in Fig. 29 with a down-range truncation of the shadow zone. In the figure, \mathcal{D}^s is (as we have already stated) the scatterer domain (i.e., the rigid object) and \mathcal{D}^{sh} is the truncated shadow domain. Again, as already stated, \mathcal{S}^i is the part of the scatterer surface \mathcal{S}^s that is illuminated by the incident beam while \mathcal{S}^{sh} is the surface of the cylindrical part of the truncated shadow domain \mathcal{D}^{sh} and \mathcal{S}^b is the surface created by the truncation process. It is to be noted that $\vec{e} \cdot d\vec{S}$ vanishes identically everywhere on \mathcal{S}^{sh} since this surface is generated by a line parallel to \vec{e} moving over the object (while maintaining tangency). This assertion is not true of \mathcal{S}^b and the ultimate neglect of this contribution must be based upon other arguments.

Based upon the above considerations it is easy to see that (14) can be replaced by

$$A(\omega, \vec{e}) = \frac{ik}{2\pi} \vec{e} \cdot [\int_{\mathcal{S}^c} d\vec{S} \exp(2ik\vec{e} \cdot \vec{r}) - \int_{\mathcal{S}^b} d\vec{S} \exp(2ik\vec{e} \cdot \vec{r})] \quad (15)$$

where \mathcal{S}^c is the composite surface made up of all the parts discussed above, i.e.

$$\mathcal{S}^c = \mathcal{S}^i + \mathcal{S}^{sh} + \mathcal{S}^b . \quad (16)$$

The second integral on the righthand side of (15) compensates for the contribution of \mathcal{S}^b in the first integral. However, if the truncation is moved a very large distance to the right, its contribution in the time domain will occur at a



SC5391.5FR

SC85-30309

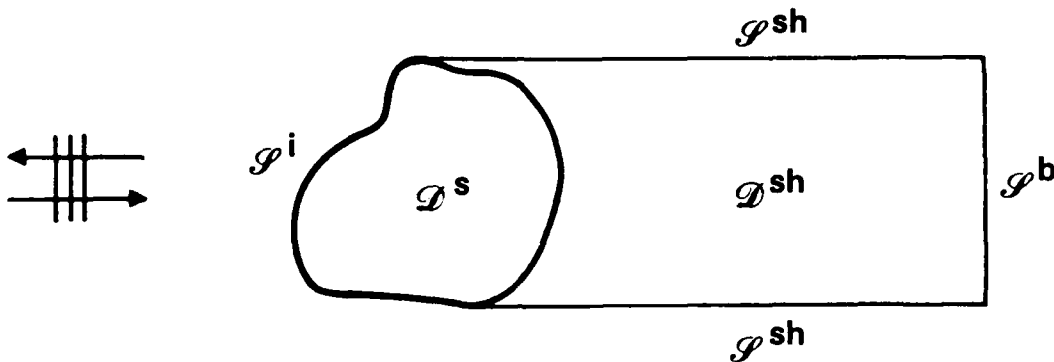


Fig. 29 Continuation of the surface integration

very late time and hence can be readily removed by time windowing. Let us assume tacitly that this is done and henceforth omit the second integral on the righthand side of (15). Applying Gauss's theorem to the remaining result we obtain

$$\begin{aligned} A(\omega, \vec{e}) &= \frac{ik}{2\pi} \int_{\mathcal{D}^c} d\vec{S} \cdot \vec{e} \exp(2ik\vec{e} \cdot \vec{r}) \\ &= \frac{ik}{2\pi} \int_{\mathcal{D}^c} d\vec{r} \nabla \cdot \vec{e} \exp(2ik\vec{e} \cdot \vec{r}) \\ &= -\frac{k^2}{\pi} \int_{\mathcal{D}^c} d\vec{r} \exp(2ik\vec{e} \cdot \vec{r}) \end{aligned} \tag{17}$$

where \mathcal{D}^c denotes the composite domain composed of the object and the truncated shadow, i.e.,

$$\mathcal{D}^c = \mathcal{D}^s + \mathcal{D}^{sh} . \tag{18}$$

Let us further assume that the truncation of the shadow domain be moved an infinite distance to the right. In any case (17) can be rewritten in terms of characteristic functions, namely



SC5391.5FR

$$A(\omega, \vec{e}) = -\frac{k^2}{\pi} \int d\vec{r} \exp(2ik\vec{e} \cdot \vec{r}) [\Gamma^S(\vec{r}) + \Gamma^{sh}(\vec{r}, \vec{e})] \quad (19)$$

where $\Gamma^S(\vec{r})$ and $\Gamma^{sh}(\vec{r}, \vec{e})$ are the characteristic functions of the object and the shadow zones, respectively, and where the integration can span any domain as long as it contains \mathcal{D}^C . The characteristic functions are defined by the relations

$$\begin{aligned} \Gamma^S(\vec{r}) &= 1, & \text{if } \vec{r} \in \mathcal{D}^S \\ &= 0, & \text{otherwise} \end{aligned} \quad , \quad (20)$$

and

$$\begin{aligned} \Gamma^{sh}(\vec{r}, \vec{e}) &= 1, & \text{if } \vec{r} \in \mathcal{D}^{sh} \\ &= 0, & \text{otherwise} \end{aligned} . \quad (21)$$

It is to be noted that the characteristic function for the shadow depends upon the incident direction \vec{e} .

It is of interest to consider that last result transformed to the time domain and the relation of the transformed result to the area function method. The arguments presented here are a minor extension of the work of F. Cohen-Tenoudji (1982). The time-domain analogue of the scattering amplitude $A(\omega, \vec{e})$ is the impulse response function $R(t, \vec{e})$ defined by

$$R(t, \vec{e}) \triangleq \frac{1}{2\pi} \int_{-\infty}^{\infty} d\omega A(\omega, \vec{e}) \exp(-i\omega t) . \quad (22)$$

With a few straightforward manipulations we obtain

$$R(t, \vec{e}) = \frac{1}{\pi c^2} \frac{d^2}{dt^2} \int d\vec{r} \Gamma^C(\vec{r}, \vec{e})(t - 2c^{-1} \vec{e} \cdot \vec{r}) . \quad (23)$$

To simplify writing we have used the characteristic function $\Gamma^C(\vec{r}, \vec{e})$ corresponding to the composite domain \mathcal{D}^C . It is easy to show that the integral in the above expression is, aside from a constant multiplier, the so-called area function of the domain \mathcal{D}^C , i.e., the domain of the object combined with its acoustical shadow. Defining ξ and s by the relation

$$\vec{r} = \vec{e} \xi + s \quad (24)$$

SC5391.5FR

we can write

$$\begin{aligned}
 & \int d\vec{r} \Gamma^C(\vec{r}, \vec{e}) \delta(t - 2c^{-1}\vec{e} \cdot \vec{r}) \\
 &= \int ds \int d\xi \Gamma^C(\xi \vec{e} + \underline{s}, \vec{e}) \delta(t - 2c^{-1}\xi) \\
 &= \frac{c}{2} \int ds \Gamma^C\left(\frac{1}{2} c t \vec{e} + \underline{s}, \vec{e}\right) \\
 &= \frac{c}{2} \mathcal{S}^C(t, \vec{e}) . \tag{25}
 \end{aligned}$$

Clearly $\mathcal{S}^C(t, \vec{e})$ is the cross-sectional area of the domain \mathcal{D}^C cut by a plane perpendicular to \vec{e} at a distance $1/2 ct$ down range from the origin. Substituting the above result into (23) gives

$$R(t, \vec{e}) = \frac{1}{2\pi c} \frac{d^2}{dt^2} \mathcal{S}^C(t, \vec{e}) \tag{26}$$

a form that is very convenient for calculation and for visualizing the scattering process in the Kirchhoff approximation.

To construct a measurement model to represent a real system producing a waveform $f(\omega, \vec{e})$ (e.g., voltage across the output terminals) from a pulse-echo, far-field scattering process we start with the expression

$$f(\omega, \vec{e}) = p(\omega) A(\omega, \vec{e}) + v(\omega, \vec{e}) \tag{27}$$

where $p(\omega)$ is the measurement system response function (MSRF) in the frequency domain and $v(\omega, \vec{e})$ is the experimental error. The MSRF is the waveform that would be produced in the absence of noise by a fictitious scatterer centered at the origin with a scattering amplitude of unity. It is to be noted that we assume that the MSRF is independent of \vec{e} . In the time domain the above result goes into

$$f(t, \vec{e}) = p(t) * R(t, \vec{e}) + v(t, \vec{e}) \tag{28}$$



SC5391.5FR

where $f(t, \vec{e})$, $p(t)$ and $v(t, \vec{e})$ are the Fourier transforms of the corresponding frequency-domain entities, i.e.,

$$\begin{pmatrix} f(t, \vec{e}) \\ p(t) \\ v(t, \vec{e}) \end{pmatrix} = \frac{1}{2\pi} \int_{-\infty}^{\infty} d\omega \exp(-i\omega t) \begin{pmatrix} f(\omega, \vec{e}) \\ p(\omega) \\ v(\omega, \vec{e}) \end{pmatrix} \quad (29)$$

Here, we are using a notation in which the function is defined in part by its arguments, e.g., $f(t, \vec{e})$ and $f(\omega, \vec{e})$ are the time and frequency domain representations of the measured waveform etc. Substituting (19) into (27) we obtain

$$f(t, \vec{e}) = \frac{1}{\pi c^2} \int d\vec{r} p''(t - 2c^{-1} \vec{e} \cdot \vec{r}) \Gamma^C(\vec{r}, \vec{e}) + v(t, \vec{e}) \quad (30)$$

where the double prime on the function denotes double differentiation with respect to the time t .

To complete the description of the measurement model one must specify the a priori statistical properties of $\Gamma^S(\vec{r})$ and $v(t, \vec{e})$. Since $\Gamma^{sh}(\vec{r}, \vec{e})$ depends solely on $\Gamma^S(\vec{r})$ and \vec{e} , its statistical properties cannot be independently specified. The formulation of a priori statistical will be further discussed in the main body of this report (i.e., Section 4.0).



Rockwell International
Science Center

SC5391.5FR

APPENDIX B

THE EFFECT OF DIFFRACTION ON MEASUREMENTS OF ULTRASONIC SCATTERING

J. M. Richardson
Rockwell International Science Center
Thousand Oaks, California 91360

and

R. B. Thompson
Iowa State University
Ames, Iowa 50011

ABSTRACT

The method of Fourier acoustics is applied to the analysis of a longitudinal-to-longitudinal wave ultrasonic scattering experiment. Explicit formulae are developed relating transducer outputs to the scattering matrix and alternatively to the scattering amplitudes. The results are applied to two cases of great experimental interest. First, a discussion is given which delineates the domains of proper application of a planar reflector and a spherical reflection calibration techniques for determining the frequency response of transducers. Second, the results are used to identify the relationship between the frequency dependence of measurements and scattering theory in the Rayleigh regime.

INTRODUCTION

In an ultrasonic measurement of the scattering of elastic waves from localized inhomogeneity, two problems of calculation present themselves. Correcting measured waveforms for the variation of transducer response with frequency is usually desirable, so that the true spectral characteristics of the scattering process can be determined. Similarly, toward this same end, it is desirable to correct for diffraction effects and material attenuation. In practice, experimentalists often make measurements on reference reflectors, such



SC5391.5FR

as planar surfaces or spherical objects, which provide a basis for partially correcting for these effects. This paper analyzes these experimental configurations and explores their domains of applicability. In addition, certain points regarding the relationship of measurements to two distinct scattering descriptions, i.e., the scattering matrix and the scattering amplitude, are described. Reciprocity arguments are applied most simply to the former, whereas scattering calculations usually predict the latter, and the distinction must be kept clear when interpreting measurements.

FOURIER ACOUSTIC ANALYSIS

The method of Fourier acoustics (FA) is applied in this section to the analysis of a longitudinal-to-longitudinal scattering experiment. For the sake of simplicity, the following assumptions are made:

1. The host medium is either a fluid, in which case transverse waves do not exist (in a practical sense), or a solid with the possibility of mode conversion producing transverse waves, which however are not detected.
2. The host medium is perfectly homogeneous, isotropic, and nonattenuative. However, our results can be easily corrected for attenuation, should it be present to a significant degree.
3. The scatterer (i.e., inhomogeneity) is assumed to be centered near the main axis of the incident beam and to be small compared with the beam width.

The set-up for the case of a pitch-catch experiment is shown in Fig. 23 above. However, to simplify the analysis, we limit our attention to the back-scatter situation appropriate for the pulse-echo case, but we still regard the receiver and transmitter as different so that results generalized to an arbitrary pitch-catch case can be made readily. As shown in the figure, we chose



Rockwell International
Science Center

SC5391.5FR

the z-axis to be the main axis of the transmitted beam. The origin O of the coordinate system is placed at the center of the face of the transmitter. A general position is denoted by

$$\vec{r} = \underline{r} + \vec{e}_z z \quad (1)$$

where r is the vector distance \perp to the z-axis, namely

$$\underline{r} = \vec{e}_x x + \vec{e}_y y . \quad (2)$$

The quantities \vec{e}_x , \vec{e}_y and \vec{e}_z are the unit vectors in the x, y and z directions, respectively. The wave field is assumed (in accordance with assumption (1) above) to be described by the scalar pressure field $p(\vec{r},t)$. The pressure is a suitable field variable for the case of wave propagation in a fluid. In an isotropic solid the pressure can also be used as the field variable for representing longitudinal waves since it is related only to the longitudinal part of the displacement field.

We can, of course, express the pressure in terms of its temporal frequency components, i.e.,

$$p(\vec{r},t) = \frac{1}{2\pi} \int_{-\infty}^{\infty} d\omega \exp(-i\omega t) p(\vec{r},\omega) . \quad (3)$$

The essence of the FA formulation is the representation of the field in terms of both temporal and spatial frequency components, but with only the spatial frequencies in the x and y directions, i.e.,

$$\underline{k} = \vec{e}_x k_x + \vec{e}_y k_y . \quad (4)$$

The total spatial frequency is clearly given by

$$\vec{k} = \underline{k} + \vec{e}_z k_z . \quad (5)$$

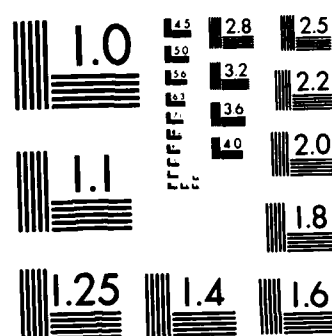
The representation in terms of k can be written

AD-A154 043 ACOUSTIC IMAGING SYSTEMS (FOR ROBOTIC OBJECT
ACQUISITION)(U) ROCKWELL INTERNATIONAL THOUSAND OAKS CA
SCIENCE CENTER J M RICHARDSON ET AL. MAR 85 SC5391.5FR
UNCLASSIFIED N00014-84-C-0085 F/G 17/1

2/2

NL





MICROCOPY RESOLUTION TEST CHART
NATIONAL BUREAU OF STANDARDS-1963-A



SC5391.5FR

$$p(\vec{r}, \omega) \equiv p(\underline{r}, z, \omega)$$

$$= \frac{1}{(2\pi)^2} \int d\underline{k} \exp(i\underline{k} \cdot \underline{r}) p(\underline{k}, z, \omega) \quad (6)$$

with the inverse relation

$$p(\underline{k}, z, \omega) = \int d\underline{r} \exp(-i\underline{k} \cdot \underline{r}) p(\underline{r}, z, \omega) \quad (7)$$

In the above expressions $d\underline{k} = dk_x dk_y$ and $d\underline{r} = dx dy$. The integrations are assumed to span all of \underline{k} -space and \underline{r} -space, respectively. We have used a notational convention in which a function is defined by its arguments, i.e., $p(\underline{k}, z, \omega)$ is a different function than $p(\underline{r}, z, \omega)$ in accordance with the relation (6).

In an isotropic host medium the propagation of longitudinal waves at a given temporal frequency ω (assumed to be positive in the remainder of this discussion) is described by the simple relation

$$|\vec{k}| \equiv k = \frac{\omega}{c} \quad (8)$$

where c is the velocity of longitudinal waves. A general solution is given by

$$p(\underline{k}, z, \omega) = p_+(\underline{k}, z, \omega) + p_-(\underline{k}, z, \omega) \quad (9)$$

where p_+ and p_- are right and left propagating waves (more precisely, fields having propagation velocities with positive and negative projections, respectively, on the z -axis). Clearly, these fields are given by

$$p_{\pm}(\underline{k}, z, \omega) = a_{\pm}(\underline{k}, \omega) \exp(\pm i \alpha z) \quad (10)$$

where

$$\alpha = \alpha(\underline{k}, \omega) = \sqrt{k^2 - |\underline{k}|^2}, \quad |\underline{k}| < k, \quad \omega > 0$$

$$= -\sqrt{k^2 - |\underline{k}|^2}, \quad |\underline{k}| < k, \quad \omega < 0. \quad (11)$$



SC5391.5FR

The case of $|k| > k$ corresponds to so-called evanescent waves which will not be of explicit concern to us in the present treatment. Propagation of a wave between z_1 and z_2 is given by

$$p_{\pm}(\underline{k}, z_2, \omega) = T_{\pm}(\underline{k}, z_2 - z_1, \omega) p_{\pm}(\underline{k}, z_1, \omega) \quad (12)$$

where the propagation transfer function is given by the simple relation

$$T_{\pm}(\underline{k}, z_2 - z_1, \omega) = \exp \pm i\alpha(z_2 - z_1) . \quad (13)$$

Thus,

$$T_+(\underline{k}, z_2 - z_1, \omega) = T_-(\underline{k}, z_1 - z_2, \omega) \quad (14)$$

and if we consider propagation from z_1 to z_2 (whatever the relations between z_1 and z_2), the transfer function is always $\exp(i\alpha|z_1 - z_2|)$.

We turn now to the specific description of each part of the system. The input of a voltage $V_T(\omega)$ into the transmitter leads to a wave output given by

$$p_+(\underline{k}, o, \omega) = H^{tr}(\underline{k}, \omega) V_T(\omega) . \quad (15)$$

The propagation through the host medium between the transmitter and the scatterer is given by

$$p_+(\underline{k}, z_s, \omega) = \exp(i\alpha z_s) p_+(\underline{k}, o, \omega) . \quad (16)$$

The scatter from the scatterer is given by

$$p_-(\underline{k}, z_s, \omega) = \int d\hat{e}^i S(\hat{e}^s, \hat{e}^i, \omega) p_+(\underline{k}', z_s, \omega) \quad (17)$$

where \hat{e}^s and \hat{e}^i are unit vectors in the incident and scattered (i.e., observer) directions, respectively, and where $S(\hat{e}^s, \hat{e}^i, \omega)$ is the so-called scattering matrix for longitudinal-to-longitudinal scattering. We require that $\hat{e}^i \cdot \hat{e}_z > 0$



SC5391.5FR

and $\hat{e}^s \cdot \hat{e}_z < 0$, conditions appropriate for a mainly forward propagating incident wave and a mainly backward propagating observed part of the scattered wave. The symbol $d\hat{e}^i$ denotes the differential solid angle in the neighborhood of the direction \hat{e}^i . In terms of the FA description \hat{e}^i , \hat{e}^s and $d\hat{e}^i$ are given by

$$\hat{e}^i = k^{-1}(\underline{k}' + \hat{e}_z d') , \quad (18)$$

$$\hat{e}^s = k^{-1}(\underline{k} - \hat{e}_z \alpha) , \quad (19)$$

where $\alpha = \alpha(\underline{k}, \omega)$ and $\alpha' = \alpha(\underline{k}', \omega)$, and

$$d\hat{e}^i = k^{-2} d\underline{k}' , \quad (20)$$

neglecting relative errors of the order of $k^{-2} |\underline{k}|^2$. Writing

$$S_b(\underline{k}, \underline{k}', \omega) = S(k^{-1}(\underline{k} - \hat{e}_z \alpha), k^{-1}(\underline{k}' + \hat{e}_z \alpha'), \omega) , \quad (21)$$

to describe backscattering in a language more compatible with FA, we can rewrite (17) in the form

$$p_-(\underline{k}, z_s, \omega) = k^{-2} \int d\underline{k}' S_b(\underline{k}, \underline{k}', \omega) \mu_+(\underline{k}', z_s, \omega) . \quad (22)$$

The scattering matrix is a symmetrical description of the scattering process in which the incident and scattered waves are treated on the same footing. For a more detailed discussion of the scattering matrix, consult the book by R.G. Newton (1).

The propagation through the host medium from the scatterer to the receiver is obviously given by

$$p_-(\underline{k}, 0, \omega) = \exp(i\alpha z_s) p_-(\underline{k}, z_s, \omega) . \quad (23)$$

Finally, the voltage output of the receiver is given by



SC5391.5FR

$$V_R(\omega) = \int d\mathbf{k} H^{rec}(\mathbf{k}, \omega) p_-(\mathbf{k}, 0, \omega) . \quad (24)$$

We do not assume any relation between the transmitter and receiver; and our final conclusions do not depend upon properties of either transducer, to say nothing of a possible interrelation. Putting the above relations together, we obtain the system equation

$$\begin{aligned} V_R(\omega) &= \int d\mathbf{k} H^{rec}(\mathbf{k}, \omega) \exp(i\alpha z_s) k^{-2} \int d\mathbf{k}' S_b(\mathbf{k}, \mathbf{k}', \omega) \\ &\times \exp(i\alpha' z_s) H^{tr}(\mathbf{k}', \omega) V_T(\omega) \end{aligned} \quad (25)$$

giving the relations between the input and output of the scattering experiment.

Although the above result has been obtained for the pulse-echo (i.e., backscatter) case, the modification for the general pitch-catch case can be readily carried out within the framework of Fourier acoustics. Another z-axis, aligned with the scatterer and receiver, describes the scattered wave. Equation (25) then stands as written except for an appropriate reinterpretation of $S_b(\mathbf{k}, \mathbf{k}', \omega)$.

APPLICATION OF RESULTS

We turn now to a brief consideration of two null experiments used for calibration (i.e., deconvolution of transducer characteristics and diffraction effects). In the first case we assume that the scatterer used above is now replaced by a perfect reflector in which case (22) is replaced by

$$p_-(\mathbf{k}, z_s, \omega) = \pm p_+(\mathbf{k}, z_s, \omega) \quad (26)$$

where the + sign denotes an acoustically hard boundary and the - sign denotes an acoustically soft boundary (i.e., a stress-free boundary). The above relation is strictly valid only for a fluid host medium or is approximately valid for a solid medium for the case of near-normal incidence. We will henceforth consider



SC5391.5FR

only the hard reflector corresponding to a rigid surface. Equation (26) corresponds to the relation

$$S_b(\underline{k}, \underline{k}', \omega) = k^2 \delta(\underline{k} - \underline{k}') . \quad (27)$$

Equation (25) now reduces to the relatively simple form

$$v_r^{\text{refl}}(\omega) = \int d\underline{k} H^{\text{rec}}(\underline{k}, \omega) \exp(i\alpha z_s) H^{\text{tr}}(\underline{k}, \omega) v_T(\omega) \quad (28)$$

which is equivalent to the case of direct transmission between transmitter and receiver separated by a distance $2z_s$. In the second case we assume a localized scatter whose characteristics are well known, namely a spherical void. In this case of course, we obtain a result identical to (25) except for the substitutions

$$v_R(\omega) \rightarrow v_R^{\text{sph}}(\omega) \quad (29)$$

$$S_b(\underline{k}, \underline{k}', \omega) \rightarrow S_b^{\text{sph}}(\underline{k}, \underline{k}', \omega) . \quad (30)$$

Of particular interest is consideration of two kinds of far-field situations. The first is one in which the transmitter and receiver are in the far-field of the localized scatterers. This situation is obviously impossible in the case where the localized scatterer is replaced by a reflector. Assuming that the transducers and localized scatterer are centered on the z-axis, the present far-field situation is equivalent to $S_b(\underline{k}, \underline{k}', \omega)$ being a slowly varying function of \underline{k} and \underline{k}' compared with the factors that lie to the left and right, respectively. Because of the above assumption of the placement of transducers (assumed to have sufficient symmetry relative to their centers), the quantities $H^{\text{rec}}(\underline{k}, \omega) \exp(i\alpha z_s)$ and $\exp(i\alpha' z_s) H^{\text{tr}}(\underline{k}, \omega)$ will be peaked at $\underline{k} = \underline{k}' = 0$ with self-cancelling oscillatory sidelobes. Equation (25) then reduces to

$$v_R(\omega) = k^{-2} C^{\text{rec}}(z_s, \omega) S_b(0, 0, \omega) C^{\text{tr}}(z_s, \omega) v_T(\omega) \quad (31)$$



SC5391.5FR

where

$$C^{tr}(z_s, \omega) = \int dk \exp(i\alpha z_s) H^{tr}(\underline{k}, \omega) \quad (32)$$

$$C^{rec}(z_s, \omega) = \int dk \exp(i\alpha z_s) H^{rec}(\underline{k}, \omega) . \quad (33)$$

In the case of the reflector null experiment (28) stands as written with no modification since here nothing is in the far-field of anything else. In the case of the spherical void null experiment, we obviously obtain

$$V_R^{sph}(\omega) = k^{-2} C^{rec}(z_s, \omega) S_b^{sph}(0,0,\omega) C^{tr}(z_s, \omega) V_T(\omega) . \quad (34)$$

With the earlier implicit assumption that the inputs $V_T(\omega)$ are the same in all cases, we obtain

$$V_R(\omega)/V_R^{sph}(\omega) = S_b(0,0,\omega)/S_b^{sph}(0,0,\omega) \quad (35)$$

demonstrating that the use of a localized scatterer in the null experiment in principle can yield a perfect deconvolution of both transducer characteristics and diffraction effects. No such deconvolution is possible in the reflector null experiment for the present far-field situation.

We consider now the second far-field situation, namely, where the scatterer is in the far-field of each transducer as well as vice versa. Here the transducer functions are slowly varying compared with $\exp(i\alpha z_s)$ which is peaked at $\underline{k} = 0$ with oscillatory side lobes. Equations (32) and (33) reduce to

$$\begin{aligned} C_A^{tr}(z_s, \omega) &= \int dk \exp(i\alpha z_s) H^{tr}(0, \omega) \\ &= \frac{2\pi ik}{z_s} \exp(ikz_s) H^{tr}(0, \omega) \end{aligned} \quad (36)$$

and

$$C^{rec}(z_s, \omega) = \frac{2\pi ik}{z_s} \exp(ikz) H^{rec}(0, \omega) . \quad (37)$$



Rockwell International
Science Center

SC5391.5FR

In evaluating $\int dk \exp(i\alpha z_s)$, we have used the Fresnel approximation

$$\alpha = \sqrt{k^2 - |\underline{k}|^2} \approx k - \frac{1}{2k} |\underline{k}|^2 \quad (38)$$

and have resorted to suitable limiting processes. Equation (31) now becomes

$$V_R(\omega) = - \frac{(2\pi)^2}{z_s^2} \exp(2ikz_s) H^{rec}(0, \omega) S_b(0, 0, \omega) H^{tr}(0, \omega) V_T(\omega) \quad (39)$$

a familiar result. Clearly, one obtains a closely analogous result for the spherical void null experiment but the ratio (35) remains the same. In the case of the reflector null experiment (28) reduces to

$$V_R^{refl}(\omega) = \frac{2\pi ik}{2z_s} \exp(2ikz_s) H^{rec}(0, \omega) H^{tr}(0, \omega) V_T(\omega) \quad (40)$$

leading ultimately to the ratio

$$V_R(\omega)/V_R^{refl}(\omega) = \frac{4\pi i}{kz_s} S_b(0, 0, \omega) . \quad (41)$$

This ratio does not have the frequency dependence of $S_b(0, 0, \omega)$ due to the factor k^{-1} . We must remember that scattering results are usually expressed in terms of the backscattering amplitude $A_b(0, 0, \omega)$, which in the present backscatter case is related to the scattering matrix in accordance with the expression

$$S_b(0, 0, \omega) = \frac{ik}{2\pi} A_b(0, 0, \omega) , \quad (42)$$

whereupon the above ratio reduces to

$$V_R(\omega)/V_R^{refl}(\omega) = - \frac{2}{z_s} A_b(0, 0, \omega) . \quad (43)$$

Thus, the ratio (43) tends to 0 as $\omega \rightarrow 0$ with the same frequency dependence as does $A_b(0, 0, \omega)$, namely proportional to ω^2 .



**Rockwell International
Science Center**

SC5391.5FR

SUMMARY

A few final remarks are necessary to put the above results into perspective. Obviously, as the frequency decreases the far-field approximations become increasingly valid; however, with different rates for different contexts. As the frequency decreases we first approach a situation in which the transducers are in the far-field of the scatterer. We then approach a second situation in which the scatterer is also in the far-fields of the transducers. In these statements, we are obviously assuming that the size of the scatterer is significantly smaller than that of the transducers. Thus, clearly deconvolution based on the spherical void null experiment is valid up to a higher value of frequency than is the deconvolution based on the reflector null experiment.



SC5391.5FR

7.0 REFERENCES

- Baker, B.B., and Copson, E.T. (1950), "The Mathematical Theory of Huygen's Principle," Clarendon Press, Oxford, 2nd ed.
- Cohen-Tenoudji, F. (1982), "Contribution of l'Etude du Probleme Inverse in Acoustique Application au Controle non Destructif des Materiaux," Ph.D. Thesis, Laboratoire de Physique de l'Ecole Normale Supérieure.
- Jarvis, R.A. (1982), Computer 15, 8.
- Schoenwald, J.S. and Martin, J.F. (1982), "Acoustic Scanning for Robotic Range Sensing and Object Pattern Recognition," in Proceedings of 1982 IEEE Ultrasonics Symposium.
- Richardson, J.M. (1985), "Exact Solution of Probabilistic Inverse Problem Pertaining to the Scattering of Elastic Waves from General Inhomogeneities," to be published in Proc. Rev. of Prog. in QNDE, 1985.
- Richardson, J.M. and Marsh, K.A. (1983a), in Proceedings of SPIE Vol. 413 "Inverse Optics," 79.
- deBilly, M. (1980), Doctoral Thesis in Physical Sciences, University of Paris VII.
- Cohen-Tenoudji, F. (1982), Doctoral Thesis in Physical Sciences, University of Paris VII.
- Richardson, J.M. and Marsh, K.A. (1983b) "Probabilistic Approach to the Inverse Problem for the Scattering of Elastic Waves from General Voids," to be published in Proc. Rev. of Prog. in QNDE, 1983.
- Hogbom, J.A. (1974), Astron. Astrophys. Suppl. 15, a417.
- Marsh, K.A. and Richardson, J.M. (1983), "Application of the Kirchhoff Approximation to Acoustic Imaging in Robotics," in Proceedings of 1983 IEEE Ultrasonics Symposium.
- Richardson, J.M. and Marsh, K.A. (1983c), "The Conjugate Vector Method in Probabilistic Inverse Problems," in Proc. Rev. of Prog. in QNDE, 1983.
- Tsai, S.J. et al. (1983), "Image Reconstruction of Flaws Using Theoretical and Experimental Impulse Response Data," in Proceedings of 1984 IEEE Ultrasonics Symposium.

END

FILMED

7-85

DTIC